RESEARCH ARTICLE SUMMARY

METABOLISM

ROS-induced ribosome impairment underlies ZAKα-mediated metabolic decline in obesity and aging

Goda Snieckute†, Laura Ryder†, Anna Constance Vind†, Zhenzhen Wu, Frederic Schrøder Arendrup, Mark Stoneley, Sébastien Chamois, Ana Martinez-Val, Marion Leleu, René Dreos, Alexander Russell, David Michael Gay, Aitana Victoria Genzor, Beatrice So-Yun Choi, Astrid Linde Basse, Frederike Sass, Morten Dall, Lucile Chantal Marie Dollet, Melanie Blasius, Anne E. Willis, Anders H. Lund, Jonas T. Treebak, Jesper Velgaard Olsen, Steen Seier Poulsen, Mary Elizabeth Pownall, Benjamin Anderschou Holbech Jensen, Christoffer Clemmensen, Zach Gerhart-Hines, David Gatfield, Simon Bekker-Jensen*

INTRODUCTION: When ribosomes stall and/or collide during mRNA translation, ribosomal surveillance mechanisms are activated. These pathways signal the presence of ribotoxic stress and coordinate the resolution of nonproductive ribosomes. The ribosome-binding and stress-sensing MAP3 kinase ZAKα is at the nexus of the ribotoxic stress response (RSR) that culminates in the activation of and signaling through the stress-associated MAP kinases p38 and JNK. The RSR pathway is nonessential, and little is known about the in vivo conditions in which translational problems occur and the contexts in which the RSR is physiologically important.

RATIONALE: Reactive oxygen species (ROS) activate p38 and JNK and impair ribosomal translation. We rationalized that these responses may be coupled, and that ROS, which is associated with a range of physiological and pathological biological transitions, is a source of RSR activation in vivo. ZAK knockout (KO) mice display a mild metabolic phenotype with leanness and decreased adiposity, suggesting that the RSR is involved in metabolic regulation. Further, p38 and JNK are involved in metabolic transitions such as the emergence of insulin resistance and liver steatosis in obesity. In the context of obesity and metabolic regulation, activation of these kinases is driven by elusive metabolic stress signals that could be mediated by any of the 21 known p38- and JNK-directed MAP3 kinases. We thus sought to investigate the potential links among ROS, RSR signaling, and metabolic regulation using cellular, zebrafish, and mouse models.

RESULTS: We confirmed that ROS activates the RSR in cellular models, associated with both stalling and collision of ribosomes. In vitro translation reactions highlighted that these effects are primarily mediated by effects on soluble translation factors, including transfer RNAs. When exposed to a pathological burst of ROS, developing zebrafish larvae deficient for the *zakα* gene were strongly protected against early lethality, likely due to prevention of RSR-induced programmed cell death. ZAK KO mice fed a high-fat high-sugar (HFHS) diet, which is associated with rapid weight gain and ROS-driven pathology in rodents, were protected against early manifestations of metabolic maladaptation, including blood glucose intolerance and liver steatosis. These phenotypes were accompanied by deregulated RSR signaling in ZAK KO mouse livers. In HFHS-fed mice, highly translated liver mRNAs displayed increased stalling and queuing of ribosomes, indicating the presence of known ZAKα-activating structures. Finally, aging in male mice is also associated with increased ROS production and metabolic deterioration manifested as impaired blood glucose intolerance, stochastic liver steatosis, and whitening of brown adipose tissue. ZAK KO mice were protected against all of these hallmarks of metabolic aging.

CONCLUSION: Our study uncovers ROS as a physiologically relevant source of translational aberrations and RSR activation. Furthermore, impaired ribosomes constitute at least a portion of the metabolic stress signals that drive unwanted metabolic maladaptation in obesity and aging. The strong protection against these reactions offered by *Zak* gene deletion in mice warrants investigation of the ZAKα kinase as a potential drug target for metabolic conditions such as nonalcoholic steatohepatitis, hypertension, and dyslipidemia. Additional work will be needed to unravel the tissue-specific contributions of RSR signaling to the above phenotypes and to identify other physiologically relevant sources of ribotoxic stress. ■

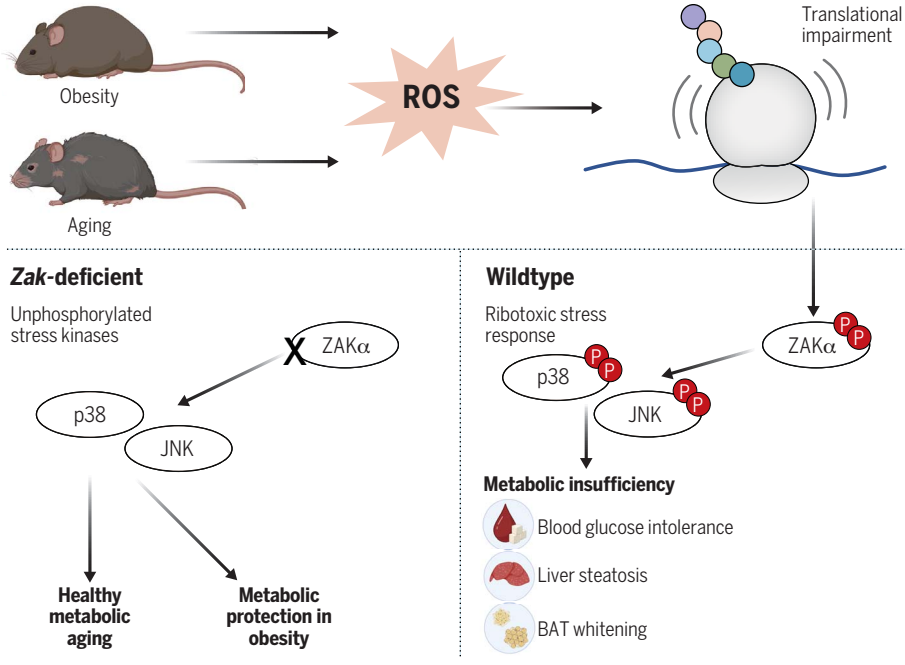

The ribotoxic stress response drives metabolic maladaptation in obesity and aging. ROS are a physiologically relevant source of translational impairment and activation of the stress kinases ZAKα, p38, and JNK. In obese and aging mice, this RSR drives metabolic maladaptation manifested by blood glucose intolerance, liver steatosis, and whitening of brown adipose tissue (BAT). [Figure created with BioRender.]

The list of author affiliations is available in the full article online.
*Corresponding author. Email: sbj@sund.ku.dk
†These authors contributed equally to this work.
Cite this article as G. Snieckute *et al.*, *Science* **382**, eadf3208 (2023). DOI: 10.1126/science.adf3208

READ THE FULL ARTICLE AT
https://doi.org/10.1126/science.adf3208

RESEARCH ARTICLE

METABOLISM

ROS-induced ribosome impairment underlies ZAKα-mediated metabolic decline in obesity and aging

Goda Snieckute[1,2]†, Laura Ryder[1,2]†, Anna Constance Vind[1,2]†, Zhenzhen Wu[1,2], Frederic Schrøder Arendrup[3], Mark Stoneley[4], Sébastien Chamois[5], Ana Martinez-Val[6], Marion Leleu[7], René Dreos[5], Alexander Russell[8], David Michael Gay[3], Aitana Victoria Genzor[1,2], Beatrice So-Yun Choi[9], Astrid Linde Basse[10], Frederike Sass[10], Morten Dall[10], Lucile Chantal Marie Dollet[10], Melanie Blasius[1,2], Anne E. Willis[4], Anders H. Lund[3], Jonas T. Treebak[10], Jesper Velgaard Olsen[6], Steen Seier Poulsen[9], Mary Elizabeth Pownall[8], Benjamin Anderschou Holbech Jensen[9], Christoffer Clemmensen[10], Zach Gerhart-Hines[10], David Gatfield[5], Simon Bekker-Jensen[1,2]*

The ribotoxic stress response (RSR) is a signaling pathway in which the p38- and c-Jun N-terminal kinase (JNK)–activating mitogen-activated protein kinase kinase kinase (MAP3K) ZAKα senses stalling and/or collision of ribosomes. Here, we show that reactive oxygen species (ROS)–generating agents trigger ribosomal impairment and ZAKα activation. Conversely, zebrafish larvae deficient for ZAKα are protected from ROS-induced pathology. Livers of mice fed a ROS-generating diet exhibit ZAKα-activating changes in ribosomal elongation dynamics. Highlighting a role for the RSR in metabolic regulation, ZAK-knockout mice are protected from developing high-fat high-sugar (HFHS) diet-induced blood glucose intolerance and liver steatosis. Finally, ZAK ablation slows animals from developing the hallmarks of metabolic aging. Our work highlights ROS-induced ribosomal impairment as a physiological activation signal for ZAKα that underlies metabolic adaptation in obesity and aging.

A high degree of metabolic flexibility allows for optimal release and utilization of energy when resources are scarce and efficient storage of energy when resources are abundant (*1*, *2*). In contemporary societies, continuous access to calorie-rich foods has caused a global obesity epidemic (*3*). In this setting, otherwise beneficious mechanisms for dynamic metabolic regulation negatively affect homeostasis. A deeper understanding of the underlying signaling pathways is needed to direct the development of new treatment principles for obesity and associated metabolic maladies (*4*). These include type 2 diabetes, nonalcoholic steatohepatitis (NASH), hypertension, and dyslipidemia. Hallmarks of early obesity-associated metabolic dysfunction include insulin resistance, pancreatic β-cell insufficiency, hepatic accumulation of lipids (steatosis), and adipose tissue hypertrophy (*5*, *6*). Similar changes occur during the process of aging (*7*), suggesting that the underlying mechanisms of metabolic alteration are related. One potential driver of metabolic dysregulation is reactive oxygen species (ROS), the production of which is increased in both obesity and aging (*8*, *9*). Elevated ROS has the potential to disturb the redox balance of cells and damage macromolecules such as proteins, DNA, and RNA. At the same time, ROS within a physiological range are prerequisite signaling molecules for homeostasis with beneficial functions (*10*, *11*). It is not clear how elevated ROS perturb metabolic functions on an organismal scale, and the underlying mechanism(s) may include indiscriminate oxidative damage to macromolecules and regulation of metabolic signaling pathways.

The stress-activated mitogen-activated protein kinases p38 and c-Jun N-terminal kinase (JNK) are activated by multiple cell stress agents such as ROS, ultraviolet (UV) light, heat stress, and mechanical perturbation. Signaling from these kinases determines diverse cellular outcomes, including cell cycle arrest, cell death, cell differentiation, stress adaptation, and inflammation (*12*). Less appreciated are the powerful roles of p38 and JNK in metabolic regulation, which have been demonstrated in a wide range of conditional knockout (KO) mouse models (*13*, *14*). These studies implicate JNK kinases in the regulation of tissue-specific and systemic insulin sensitivity, hepatic lipid deposition, and production of adipokines, among others (*14*). Among its many roles in metabolic regulation, p38 regulates β cell survival (*15*) and key processes in adipose tissues such as thermogenesis and lipolysis (*16*). Activation of p38 and JNK is associated with obesity and metabolic syndrome, and targeting of these kinases or nonessential components of their signaling pathways has been proposed as a therapeutic approach for the treatment or prevention of these metabolic diseases (*13*, *17*). In particular, the protection of JNK-deleted mice against high-fat diet–induced insulin resistance and hepatic steatosis (*14*, *18*, *19*) points to MAP kinase signaling pathways as key regulators of metabolic flexibility and drivers of metabolic decline.

MAP kinases are activated through signal transduction cascades involving upstream MAP kinase kinases (MAP2Ks) and MAP kinase kinase kinases (MAP3Ks) (*12*). The most upstream of these components, the MAP3Ks, are a group of 21 human kinases, of which we only know the activation mechanisms and signals for a few. One MAP3K that has recently attracted interest is ZAKα, which interacts with the ribosome and is a sensor of translational impairment (*20*). ZAKα binds to ribosomes by virtue of two C-terminal ribosome-binding domains (*21*) and is activated by perturbations such as stalling and/or collision of ribosomes (*22*, *23*). This pathway for monitoring ribosomal function and converting ribosomal aberrations into p38 and JNK activation is known as the ribotoxic stress response (RSR) (*24*). Our knowledge about the function of the RSR has been gleaned in mammalian cell lines with treatments such as ribotoxin enzymes (including ricin, Shiga toxin, and α-sarcin, all of which have pathological relevance as human toxins), antibiotics (including anisomycin and cycloheximide), or UV irradiation (*25*, *26*), which damage or chemically inhibit the ribosome or damage mRNA templates, respectively. Except for UVB irradiation of keratinocytes in the skin (*27*), these treatments neither offer much insight into the physiological sources of ribosome stalling, ribosome collision, and RSR activation nor provide any clues as to the physiological roles of this signaling pathway in the context of a whole organism. Here, we show that ROS is a powerful activator of ZAKα and downstream RSR signaling, and that a ROS-generating obesogenic diet is associated with altered ribosomal elongation dynamics in the mouse liver. In the context of obesity and aging, the RSR pathway mediates well-known but unwanted metabolic transitions such as deregulated glucose tolerance and liver steatosis. Our work offers mechanistic insights into metabolic regulation by MAP kinase signaling and

[1]Center for Healthy Aging, Department of Cellular and Molecular Medicine, University of Copenhagen, DK-2200 Copenhagen, Denmark. [2]Center for Gene Expression, Department of Cellular and Molecular Medicine, University of Copenhagen, DK-2200 Copenhagen, Denmark. [3]Biotech Research and Innovation Center, University of Copenhagen, DK-2200 Copenhagen, Denmark. [4]MRC Toxicology Unit, University of Cambridge, Cambridge CB2 1QR, UK. [5]Center for Integrative Genomics, University of Lausanne, 1015 Lausanne, Switzerland. [6]Mass Spectrometry for Quantitative Proteomics, Proteomics Program, The Novo Nordisk Foundation Center for Protein Research, Faculty of Health and Medical Sciences, University of Copenhagen, DK-2200 Copenhagen N, Denmark. [7]Bioinformatics Competence Center, Ecole Polytechnique Fédérale de Lausanne and University of Lausanne, CH-1015 Lausanne, Switzerland. [8]Department of Biology, University of York, York YO10 5DD, UK. [9]Department of Biomedical Sciences, University of Copenhagen, DK-2200 Copenhagen, Denmark. [10]Novo Nordisk Foundation Center for Basic Metabolic Research, Faculty of Health and Medical Sciences, University of Copenhagen, DK-2200 Copenhagen, Denmark.
*Corresponding author. Email: sbj@sund.ku.dk
†These authors contributed equally to this work.

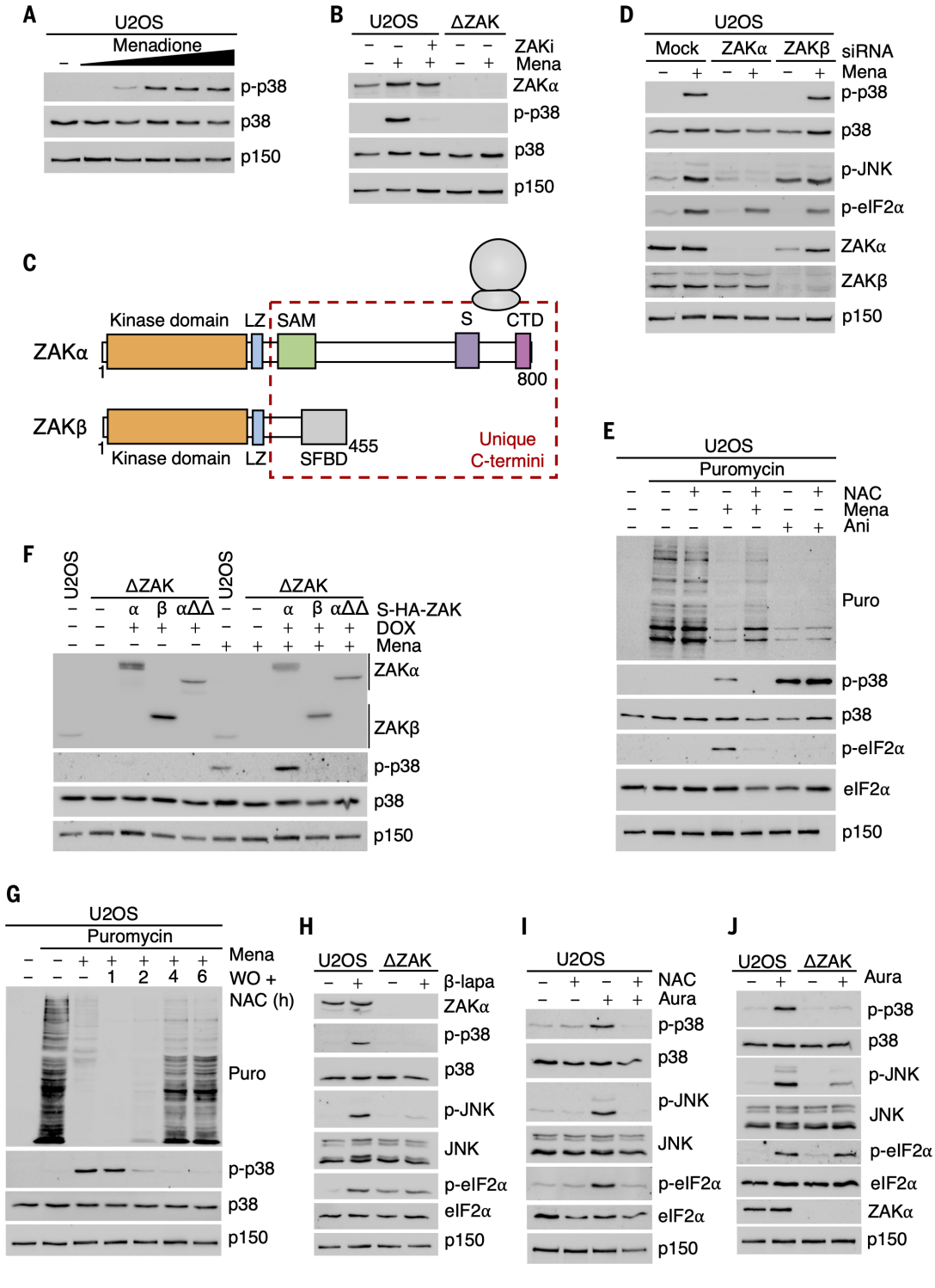

Fig. 1. ROS inhibit translation and activate the RSR. (**A**) U2OS cells were treated with increasing concentrations of menadione (25, 50, 150, 250, and 500 μM for 1 hour). Lysates were analyzed by immunoblotting with the indicated antibodies. (**B**) WT U2OS cells or U2OS cells deleted for ZAK (ΔZAK) were treated with a ZAK inhibitor (ZAKi, 2 μM) and menadione (Mena, 250 μM for 1 hour). Lysates were analyzed as in (A). (**C**) Schematic of ZAK protein isoforms. LZ, leucine zipper; SAM, sterile alpha-motif; S, sensor domain; CTD, C-terminal domain; SFBD, stress fiber binding domain. (**D**) U2OS cells were transfected with control (mock) small interfering RNA (siRNA) or siRNAs targeting the α or β isoforms of ZAK. Cells were treated with menadione (250 μM for 1 hour), and lysates were analyzed as in (A). (**E**) U2OS cells were pretreated with NAC (10 mM for 1 hour) followed by addition of menadione (250 μM for 1 hour) or anisomycin (Ani, 1 μg/ml for 1 hour) as indicated. Puromycin (10 μg/ml) was added to the culture 10 min before harvest, and lysates were analyzed by immunoblotting with the indicated antibodies. (**F**) U2OS cells, ΔZAK cells, and ΔZAK cells rescued with WT and mutated forms of ZAKα and WT ZAKβ were treated as in (D) [αΔΔ is a deletion of the "S" and "CTD" domain in (C)]. Lysates were analyzed as in (A). (**G**) U2OS cells were treated with menadione (250 μM for 1 hour) followed by washout (WO) in the presence of NAC (10 mM) for the indicated times. Cells were pulse treated with puromycin (10 μg/ml, 10 min) before harvest as in (E). Lysates were analyzed as in (A). (**H**) Cells from (B) were treated with ROS-generating β-lapachone (β-lapa, 20 μM for 1 hour) and lysates were analyzed as in (A). (**I**) U2OS cells were pretreated with NAC (10 mM for 1 hour), followed by addition of auranofin (Aura, 5 μM for 1 hour) as indicated. Lysates were analyzed as in (A). (**J**) Cells from (B) were treated with auranofin (5 μM for 1 hour), and lysates were analyzed as in (A).

points to the ribosome as a hitherto unappreciated sensor of metabolic stress.

Results

ROS inhibit protein synthesis and activate the RSR

Oxidative stress and ROS are both inhibitory to translation (*28*) and lead to activation of p38 and JNK (*29*). In search of a potential link between these effects, we treated U2OS cells with a p38-activating dose of menadione, which causes intracellular superoxide radical generation through a futile reduction-oxidation cycle (Fig. 1A). p38 activation was completely abrogated both by an inhibitor of ZAK kinase activity and by CRISPR-mediated inactivation of the *Zak* gene (Fig. 1B). Menadione appeared to activate the RSR, becausae p38 activation required the ribosome-binding α-isoform, but not the unrelated β-isoform, of ZAK (Fig. 1, C and D). In further support of this notion, we found that menadione strongly inhibited bulk

translation in a puromycin-incorporation assay (Fig. 1E) and required functional ribosome-binding domains in ZAKα for p38 activation (Fig. 1F). These effects were reversible, because cells both resumed translation and silenced p38 activity, albeit with some delay, when menadione was washed out in the presence of the ROS scavenger N-acetylcysteine (NAC) (Fig. 1G). Menadione also activated the integrated stress response (ISR), as evidenced by eIF2α phosphorylation, and all of the above effects could be circumvented by preincubation of cells with NAC (Fig. 1E and fig. S1A). These effects of ROS were not restricted to menadione, because we found that the redox cycling agent β-lapachone and the thioredoxin reductase inhibitor auranofin similarly reduced ribosomal output and activated both p38 and JNK in a ZAK-dependent and NAC-reversible manner (Fig. 1, H to J, and fig. S1, B to D). On the basis of these results, we conclude that ROS exposure acutely triggers RSR signaling in cells.

ROS induce ribosome stalling in vivo and impair translation in vitro

ZAKα responds to both stalling and collision of ribosomes (*22*, *23*). To understand the mechanistic basis of ROS-induced RSR activation, we analyzed ribosome collisions in cells by digesting polysomes with micrococcal nuclease (MNase) and resolving the collided ribosomes on a sucrose gradient (*30*). Upon treatment of cells with menadione for 30 min or 1 hour, this approach did not reveal an increase in MNase-resistant polysome peaks, which are indicative of stacked ribosomes (Fig. 2A and fig. S1E, left). However, treatment of U2OS cells with β-lapachone for 30 min produced a small increase in collided ribosomes (fig. S1F, left). These results were in clear contrast to anisomycin treatment, which gave rise to substantial amounts of ribosome collisions (fig. S1G), as previously reported (*22*, *30*). We and others have previously reported that amino acid deprivation results in stalling of elongating ribosomes, but these stalled ribosomes are only converted to collisions upon inhibition of the ISR (*30*, *31*). Because ROS also activate the ISR (Fig. 1), we wondered if this response also limits ribosome collisions in response to menadione and β-lapachone. Treatment of cells with the pan-ISR inhibitor ISRIB did stimulate low levels of ribosome collision at 30 min after both menadione and β-lapachone addition (Fig. 2A and fig. S1F, right, and H), but these effects were transient and largely undetectable at the 1- and 2-hour time points (fig. S1E). These data suggest that cells react acutely to ROS-generating agents with both stalling and collision of ribosomes, and that high levels of ROS themselves interfere with translation initiation at later time points. Indeed, both menadione and β-lapachone treatments were accompanied by a time-dependent loss of polysomes that could not be reversed by ISRIB (fig. S1, I and J). Targeting of initiating 80*S* ribosomes with harringtonine resulted in the fast runoff of elongating ribosomes (Fig. 2B, left), as previously shown (*32*). This runoff was impeded for the remaining translating ribosomes in menadione-treated cells (Fig. 2B, right), further supporting that ROS slow down and/or stall elongating ribosomes. Consistent with the above, and in contrast to anisomycin treatment, ribosome-enriched pellets from menadione-treated cells were negative for all biochemical markers of collided elongating [EDF1 (*33*, *34*), ubiquitylated RPS10 and ZNF598 (*35*, *36*)] and initiating [ubiquitylated RPS2 (*37*, *38*)] ribosomes (fig. S2, A and B). In addition, the endoplasmic reticulum (ER) stress–responsive kinase PERK, and not ribosome-associated GCN2, appeared to be the more relevant eIF2α kinase upon treatment of cells with menadione and auranofin (Fig. 2C and fig. S2C). These and previous (*23*) data indicate that activation of ZAKα upon acute ROS exposure can occur independently of widespread ribosome collision and may thus largely depend on stalling and slowing of individual ribosomes (fig. S2D). Our results also highlight that the triggers of ER stress and ribotoxic stress are overlapping. Indeed, the ER stress–inducing agent thapsigargin strongly repressed bulk ribosomal translation and induced ZAKα activation (fig. S2, E to G).

ROS have the potential to damage nucleotides in DNA as well as RNA, and oxidative modification of both ribosomal RNA (rRNA) and mRNA bases has previously been associated with translational impairment (*39*). To understand which components of the translation process are sensitive to ROS, we developed a tripartite in vitro translation system from lysates of HeLa cells (Fig. 2D). This cell line also displayed menadione-induced and NAC-reversible translational inhibition and p38 activation (fig. S2, H and I). Our approach consisted of isolating ribosomes from one culture of HeLa cells and a ribosome-free cytoplasmic fraction containing transfer RNAs (tRNAs) and initiation and elongation factors from another, which only upon combination supported translation of an in vitro–transcribed luciferase-encoding mRNA (Fig. 2D and fig. S2J). To introduce oxidative damage to the in vitro translation system, we treated only one of the three components at a time with hydrogen peroxide for 10 min. To prevent carryover effects, we subsequently neutralized the hydrogen peroxide with catalase before combining the fractions and determining the extent of luciferase protein production. To our surprise, the ability of ribosomes or luciferase mRNA to support translation was not impaired by hydrogen peroxide treatment, rather, it was the cytoplasmic fraction that was exquisitely sensitive to oxidative damage (Fig. 2E). This result was in stark contrast to collision-causing UVB irradiation, which negatively affected exclusively the mRNA component (Fig. 2F), as previously described (*22*). We also prepared the ribosomal and cytoplasmic fractions directly from menadione- and NAC-treated HeLa cells (Fig. 2G). In these experiments as well, our results indicated that the cytoplasmic fraction, but not the ribosomal fraction, contained one or more soluble ROS-sensitive components (Fig. 2, H and I). Using a biotin switch assay (*40*), we did not find biochemical evidence for cysteine oxidation in a number of relevant translation initiation and elongation factors after menadione treatment (fig. S3A). Global inspection of tRNA integrity also did not indicate large-scale degradation of the tRNA pool in the cytoplasmic fraction (Fig. 2J). However, Northern blotting for the tRNA Arg-TCT revealed marked cleavage and fragmentation, which was induced by menadione and reversed by NAC (Fig. 2K). Similar but much weaker effects were observed for the tRNAs Leu-CAA, Gly-GCC, and iMet-CAT (fig. S3, B to D), without an apparent effect on tRNA charging (fig. S3E). Angiogenin is a tRNA-cleaving RNase that is activated upon a multitude of cellular stress insults to produce translation-inhibiting tRNA fragments (*41*, *42*). Activation of angiogenin by menadione and ensuing tRNA cleavage was recently demonstrated (*43*). Although these effects may not be the only relevant ones, we conclude that ROS-inducing agents interfere with translation in vivo and in vitro and activate ZAKα and the RSR.

Additive contributions from ZAKα and ASK1 underlie ROS-induced p38 and JNK activation

When challenged with menadione, p38 activation occurred in two distinct waves, one starting at 5 min after exposure and peaking at 10 to 15 min, and another starting at 45 min and peaking at 1 to 2 hours (Fig. 3A). Only the second of these peaks coincided with ISR activation, translation shutdown, and appearance of oxidized proteins (Fig. 3A and fig. S3F). When analyzing U2OS cells deleted for the *ZAK* and *ASK1* genes either individually or in combination, the ROS-activated MAP3K ASK1 (*44*) appeared to be involved only in the first of these responses, whereas ZAKα was exclusively required for the second wave (Fig. 3B). These data imply that ASK1 is a faster responder to oxidative stress, and that damage to macromolecules and ribosomal impairment precedes activation of the RSR. We also challenged our U2OS cells with hydrogen peroxide and observed a partial dependency for both ZAK and ASK1 kinase activity for stress-associated MAPK activation (fig. S3G). Our results add to the existing knowledge about ASK1 as a ROS-activated MAP3K and highlight ZAKα as a nexus in a parallel pathway that relays ROS-induced translational impairment toward MAPK signaling (Fig. 3C).

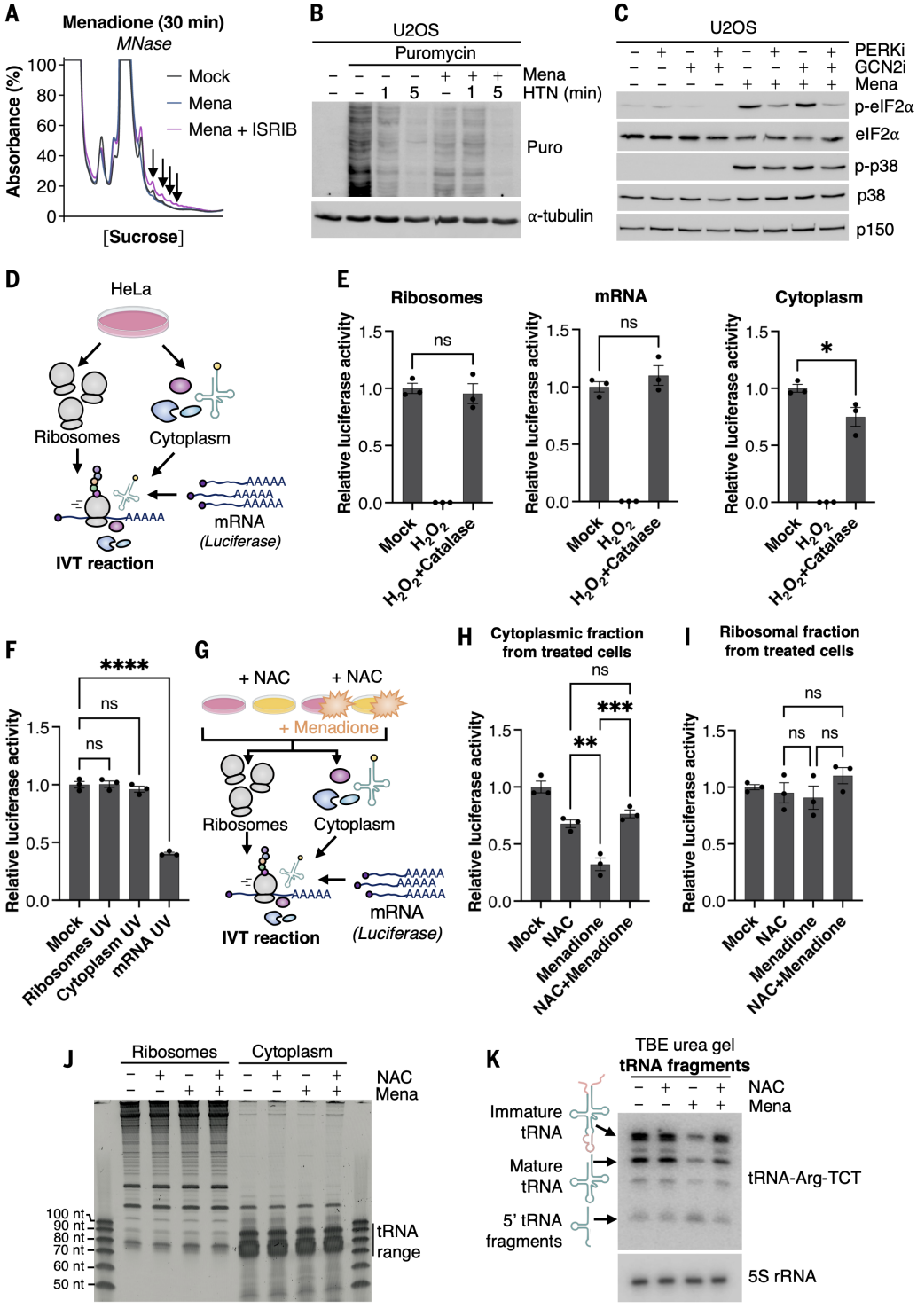

Fig. 2. ROS-induced ZAKα activation is associated with ribosome stalling and collision. (**A**) U2OS cells were treated with menadione (Mena, 250 μM for 30 min) and ISRIB (200 nM). Lysates were digested with MNase and separated on a linear sucrose gradient. Arrows highlight UV peaks that are indicative of increased ribosome collision. (**B**) U2OS cells were pretreated with menadione (250 μM for 1 hour) as indicated and harringtonine (HTN, 2 μg/ml) for the indicated times to induce ribosome run-off. Puromycin (10 μg/ml) was added to the culture for 5 min before harvest (but after HTN incubation time) and lysates were analyzed by immunoblotting with the indicated antibodies. (**C**) U2OS cells were treated with menadione (250 μM for 1 hour) and inhibitors (i, 1 μM) against PERK and GCN2 as indicated. Lysates were analyzed as in (B). (**D**) Schematic of tripartite in vitro translation (IVT) approach. Ribosomes, ribosome-free cytoplasm, and mRNA can be individually treated before combination. (**E**) The three fractions from (D) were individually treated with hydrogen peroxide (10 min) and neutralized by the addition of catalase as indicated. Translation efficiency in the combined reaction was determined by luciferase assay. (**F**) As in (E), except that the fractions were individually irradiated with UVB (500 J/m^2) before in vitro translation. (**G**) Schematic of modified tripartite IVT assay. In contrast to (D), HeLa cells were pretreated with NAC (10 mM for 1 hour), followed by addition of menadione (250 μM for 1 hour) before purification of fractions. (**H**) Combined IVT reactions with treated with ribosome-free cytoplasm from (G). (**I**) As in (H), except that treated ribosomes from (G) were used. All values indicate luciferase activity normalized to the control. For (E), (F), (H), and (I), data are plotted as means, and all error bars represent the SEM (n = 3 biological replicates). ns, nonsignificant; *$P \le 0.05$; **$P \le 0.01$; ***$P \le 0.001$; ****$P \le 0.0001$ by Student's t test for two groups and one-way ANOVA with Tukey's post hoc test for more than two groups. (**J**) Whole-cell RNA isolated from HeLa cell fractions from (G) was separated on urea agarose gel and stained for RNA. nt, nucleotides. (**K**) Northern blot for tRNA-Arg-TCT on RNA samples from (J). Schematic of tRNA intermediates corresponding to distinct bands are shown on the left side of the blot.

ZAKα mediates ROS-induced death in zebrafish larvae

To probe the organismal consequences of ROS-induced RSR signaling, we turned to zebrafish as a model organism. Zebrafish is amenable to CRISPR-mediated genetic manipulation and is an attractive organism for developmental studies because of its fast extrauterine development (*45*). Whereas mammals contain a single *Zak* gene that encodes two distinct splice variants (Fig. 1C), zebrafish express clear orthologs of ZAKα and ZAKβ from two independent genes (fig. S3H). We thus proceeded to interrupt these two genes in zebrafish (Fig. 3D) and generated single- and double-KO animals (Fig. 3E). The genetically introduced deletions to interrupt the open reading frames of the two paralogs also reduced their mRNA

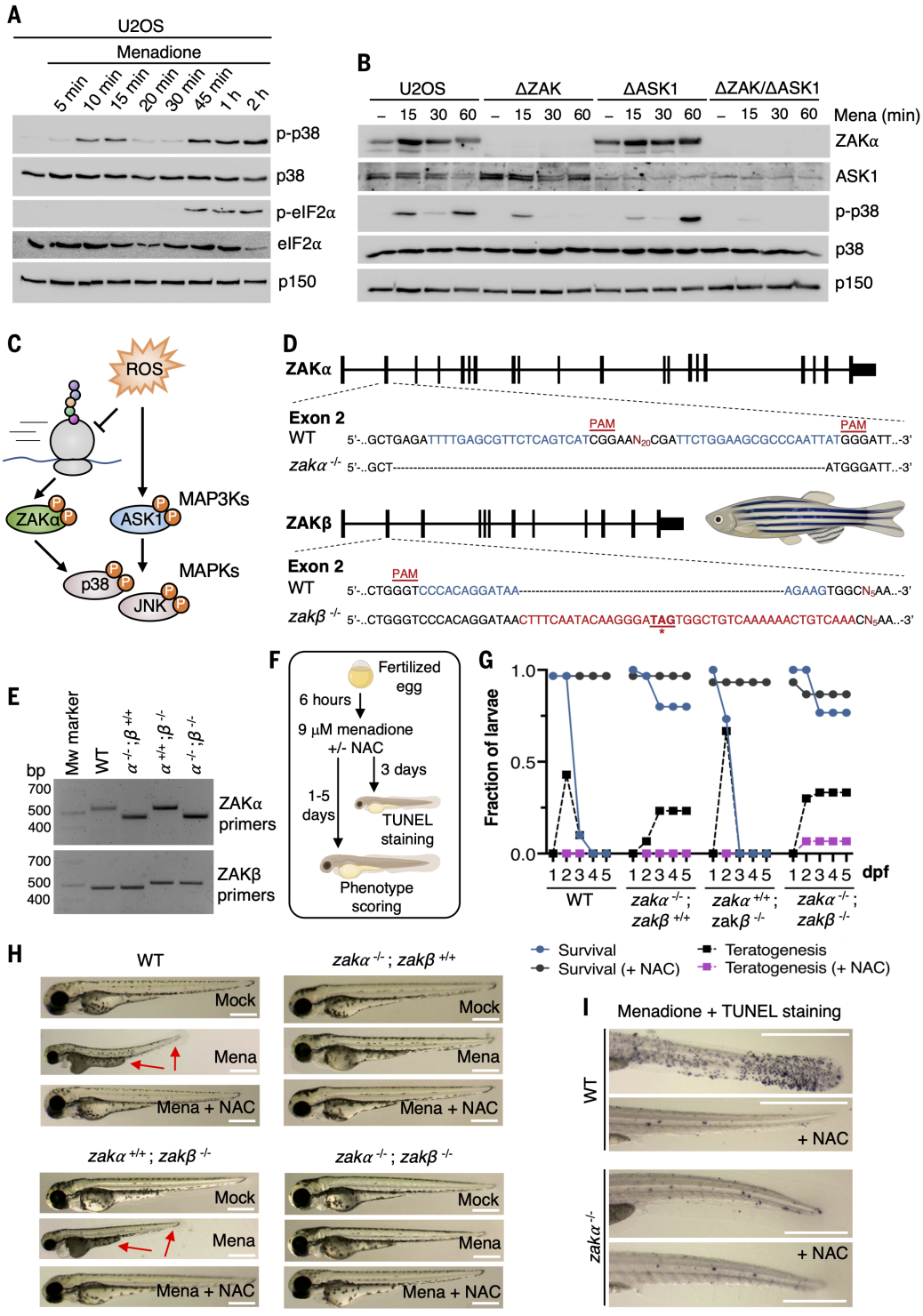

Fig. 3. ZAKα mediates menadione-induced apoptosis and death in zebrafish. (**A**) U2OS cells were treated with menadione (250 μM) for the indicated times. Lysates were analyzed by immunoblotting with the indicated antibodies. (**B**) U2OS cells individually deleted for ZAK (ΔZAK), ASK1 (ΔASK1), and both (ΔZAK/ΔASK1) were treated with menadione (250 μM) for the indicated times. Lysates were analyzed as in (A). (**C**) Model of ROS-induced activation of p38 and JNK kinases by parallel sensing mechanisms. ZAKα responds to ROS-induced impairment of ribosomal translation (left), whereas ASK1 activity is directly controlled by intracellular ROS levels (right). (**D**) Genomic location of guide RNA sequences (blue) and derived knockout alleles in exon 2 of zebrafish *zakα* (top) and *zakβ* (bottom) genes. A 33-bp insertion in mutated *zakβ* is highlighted in red, with the position of an in-frame STOP codon underlined and in bold. PAM, protospacer adjacent motif. (**E**) Genotyping of WT and CRISPR-modified alleles of *zakα* and *zakβ* genes from (D). A single zebrafish larva per genotype was lysed and submitted to genomic PCR with the indicated primer pairs. Amplified bands were resolved by agarose gel electrophoresis. (**F**) Schematic of experiments with menadione treatment of zebrafish larvae. Zebrafish eggs were incubated in the presence of menadione (9 μM) and/or NAC (60 μM) from 6 hours postfertilization and up to 5 days. Larvae were scored as dead or alive once per day, and the number of fish with developmental phenotypes was determined. For detection of apoptosis, larvae treated for 3 days were fixed and subjected to TUNEL staining. (**G**) Thirty zebrafish larvae with each of the indicated genotypes were treated and scored as in (F). Only larvae with cardiac arrest were scored as dead. The data shown are from one representative experiment out of the three performed. dpf, days post fertilization. (**H**) Representative images of larvae from (G) at day 3. WT fish treated with menadione (Mena) presented with darkened yolk sac, cardiac edema, and short kinked tails (red arrows). The addition of NAC or deletion of *zakα* largely obliviated these pathologies. (**I**) WT and *zakα*$^{-/-}$ larvae were treated as in (F) for 3 days, fixed, and subjected to TUNEL staining. Photographs show representative images of the tail part of the larvae. All scale bars, 500 μm.

abundances, with *zakβ* knockout additionally affecting *zakα* expression (50% reduction) (fig. S3I).

Exposure of fertilized wild-type (WT) zebrafish eggs to menadione resulted in death (scored as cardiac arrest) of most of the larvae after 3 to 4 days (Fig. 3, F and G). This was preceded by the appearance of a range of developmental phenotypes such as edema of the yolk sac and heart, curved spine or tail, and decreased length (Fig. 3H). All of these marked effects could be attributed to pathological ROS generation because they were prevented by the coadministration of NAC in the culture water (Fig. 3, G and H). Although *zakβ*$^{-/-}$ fish were

similarly sensitive to the effects of menadione, *zakα*$^{-/-}$ and double-KO larvae were largely resistant to death and to the appearance of pathological phenotypes (Fig. 3, G and H). Menadione-induced pathology was associated with apoptotic cell death, as visualized by TUNEL-positive cells in the tails of WT larvae, and this effect could also be prevented by co-administration of NAC or *zakα* deletion (Fig. 3I). We conclude that ZAKα, but not ZAKβ, responds to ROS in an organismal setting and that *zakα*$^{-/-}$ zebrafish larvae are quite protected, at least in the short term, against the harmful effects of a pathological burst of ROS.

ZAK$^{-/-}$ *mice are protected against metabolic dysfunction when fed a calorie-rich diet*

Examining the relative expression levels of *ZAKα* and *ASK1* transcripts across human tissues, we observed that the liver contained relatively little *ASK1* mRNA while at the same time being one of the very few tissues in which the expression of *ZAKα* exceeds that of *ZAKβ* (fig. S3J; data from the GTExPortal: https://gtexportal.org/). Reanalysis of a recent tissue-resolved draft of the mouse proteome (*46*) also indicated that the ZAKα protein is expressed at higher levels than ASK1 in several metabolic organs, including the liver (fig. S3K). We proceeded by subjecting male WT and ZAK$^{-/-}$ mice to a diet rich in lipids and sugar (high-fat, high-sugar: HFHS) for 25 weeks, only interrupted by intraperitoneal glucose tolerance tests (ipGTT) and magnetic resonance (MR) scans to determine body composition (Fig. 4A). This diet is known to result in increased adiposity, insulin resistance, and liver steatosis (*47*), with increased ROS generation serving, at least in part, as an underlying pathological driver (*48*). As we previously reported (*49*), the starting weights of the male ZAK$^{-/-}$ mice were slightly lower than those of their WT littermates (fig. S4A). Initial weight gain was also somewhat delayed in ZAK$^{-/-}$ mice when shifted from chow to HFHS diet, but mice then proceeded to gain weight in a largely genotype-independent manner (Fig. 4B) and ingested similar amounts of food throughout the experiment (fig. S4B). MR scanning revealed that fat mass increased as expected in WT mice (fig. S4C), but with some retardation in ZAK$^{-/-}$ mice (fig. S4C), in both cases with a relatively constant lean mass (fig. S4D). In WT mice, HFHS feeding also resulted in the expected loss of blood glucose control as determined by ipGTT, being evident at 8 weeks and exacerbated at 19 weeks (Fig. 4C). Conversely, HFHS-fed ZAK$^{-/-}$ mice were well protected against such functional metabolic decline and performed similarly to chow-fed mice in ipGTT at the 8-week time point (Fig. 4C, top versus middle). At the 19-week time point, ZAK$^{-/-}$ mice appeared to have developed a certain degree of glucose intolerance, albeit this was less pronounced than in the WT (Fig. 4C, bottom). Consistent with this, ZAK$^{-/-}$ mice exhibited less insulin resistance at the 19-week time point, as evidenced by 50% reduced HOMA-IR (Homeostatic Model Assessment for Insulin Resistance) values (Fig. 4D and fig. S4, E and F). In contrast to glucose intolerance, frank insulin resistance, assessed by HOMA-IR or an insulin challenge test developed over a longer time span (*50*). Consistent with this and in a distinct mouse cohort, WT mice appeared insulin sensitive and thus not significantly different from ZAK$^{-/-}$ mice after 8 weeks of HFHS feeding (Fig. 4E), thus not fully recapitulating the reported phenotype of JNK-deficient mice (*51*). Liver weights measured after euthanasia were similar between WT and ZAK$^{-/-}$ mice (fig. S4G), yet the hepatic triglyceride content was ~50% lower in HFHS-fed ZAK$^{-/-}$ mice despite indistinguishable serum triglyceride levels (Fig. 4F and fig. S4H). This difference also manifested as lower steatosis grades in ZAK$^{-/-}$ livers (Fig. 4, G and H).

The observed early protection against diet-induced glucose intolerance and the long-term protection against hepatic steatosis in ZAK$^{-/-}$ over WT mice despite a similar whole-body insulin sensitivity at 8 weeks of feeding prompted us to search for alternative explanations for the metabolic protection offered by *Zak* deletion. First, we subjected WT and ZAK$^{-/-}$ mice on an HFHS diet for 10 weeks to a glucose-tracing experiment using tritiated 2-deoxy-D-glucose (2DG). Mice were euthanized 1 hour after injection, and uptake of radioactive glucose was determined in several central and peripheral tissues (fig. S4I). Consistent with our glucose challenge experiments (Fig. 4C), radioactivity was cleared faster from the bloodstream of ZAK$^{-/-}$ mice (fig. S4J, top left), although uptake of 2DG and its conversion to 2DG-6-phosphate (2DG6P) at the end point was similar between genotypes (fig. S4J, remaining panels). These results indicate an equal total capacity for glucose uptake in WT and ZAK$^{-/-}$ tissues after 60 min, with potential kinetic effects at earlier time points. Second, we placed mice of both genotypes that had been fed chow or HFHS for 6 weeks in metabolic chambers for 1 week and monitored their movement, consumption of O_2, and production of CO_2 (fig. S5A). Locomotor activity and energy expenditure were largely independent of genotype (for within-genotype variance = 0.0022 kcal/h^2, see fig. S5, B to D; for between-genotype variance = 0.00027 kcal/h^2, see fig. S5C). However, we observed a substantial increase in the respiratory exchange ratio in ZAK$^{-/-}$ mice over WT when they were fed the regular chow diet (fig. S5, E to G). This result indicates a preferred utilization of carbohydrates over lipids as energy sources in ZAK$^{-/-}$ mice, likely as a consequence of the reduced adiposity of these animals (*23*). This readout was only observable in chow-fed mice, and the pronounced HFHS-induced suppression of respiratory exchange ratio exceeded that of the two genotypes, thus impeding further interrogation of obese mice.

To evaluate the contribution of ROS to metabolic phenotypes associated with ZAK KO, we combined HFHS feeding with 10 g per liter NAC supplementation in the drinking water. IpGTT assays were performed at 5 and 10 weeks, and mice were euthanized after 12 weeks of treatment (fig. S6A). In this experiment, weight gain was also initially delayed in ZAK$^{-/-}$ mice and was further reduced by the high dose of NAC (fig. S6B). IpGTT assays confirmed the progressive development of glucose intolerance and HOMA-IR elevation in WT mice, whereas ZAK$^{-/-}$ mice were fully protected against such metabolic decline after both 5 and 10 weeks of HFHS feeding (fig. S6, C to G). NAC supplementation completely nullified these differences between genotypes in terms of ipGTT (fig. S6, C and D), fasting insulin levels (fig. S6F), and HOMA-IR (fig. S6G). Conversely, NAC supplementation only partly improved the liver steatosis grade in WT mice and did not appear to offer the same protection as ZAK KO against this outcome (fig. S6, H and I). Our results indicate that RSR signaling activated by ROS and other sources of ribosomal impairment mediates at least some aspects of metabolic adaptation to an obesogenic diet.

Phospho-proteomic analysis reveals deregulation of MAPK signaling in livers of ZAK$^{-/-}$ *HFHS-fed mice*

We used phosphoproteomics to investigate signaling toward p38 and JNK kinases in livers of mice fed HFHS for 5 weeks and euthanized during the dark phase, when hepatic ROS levels are maximal (*52*) (Fig. 5A). We identified ~5500 unique proteins and ~12,500 unique phosphorylation sites (tables S1 and S2). Principal component analysis (PCA) revealed little separation of samples at the protein level (fig. S7A) but a clear separation and clustering according to both genotype and diet at the level of phosphorylation sites (Fig. 5B). We used this dataset to investigate phosphorylation changes annotated as regulatory on all recorded MAPK, MAP2K, and MAP3K components (fig. S7B). This analysis revealed HFHS- and *Zak*-dependent regulation of activation-associated phosphorylation sites on several components of p38 and JNK signaling cascades. A finer analysis of the relevant phosphopeptides across all conditions revealed a decrease in activation-associated phosphorylation of JNK2 (MAPK9-Y185) upon HFHS feeding of ZAK$^{-/-}$ but not WT mice (Fig. 5C, fig. S7C, and table S2). However, Western blot analysis on the same liver samples did not indicate decreased HFHS-induced JNK phosphorylation in ZAK$^{-/-}$ mice (Fig. 5D). A portion of the HFHS-induced RSR

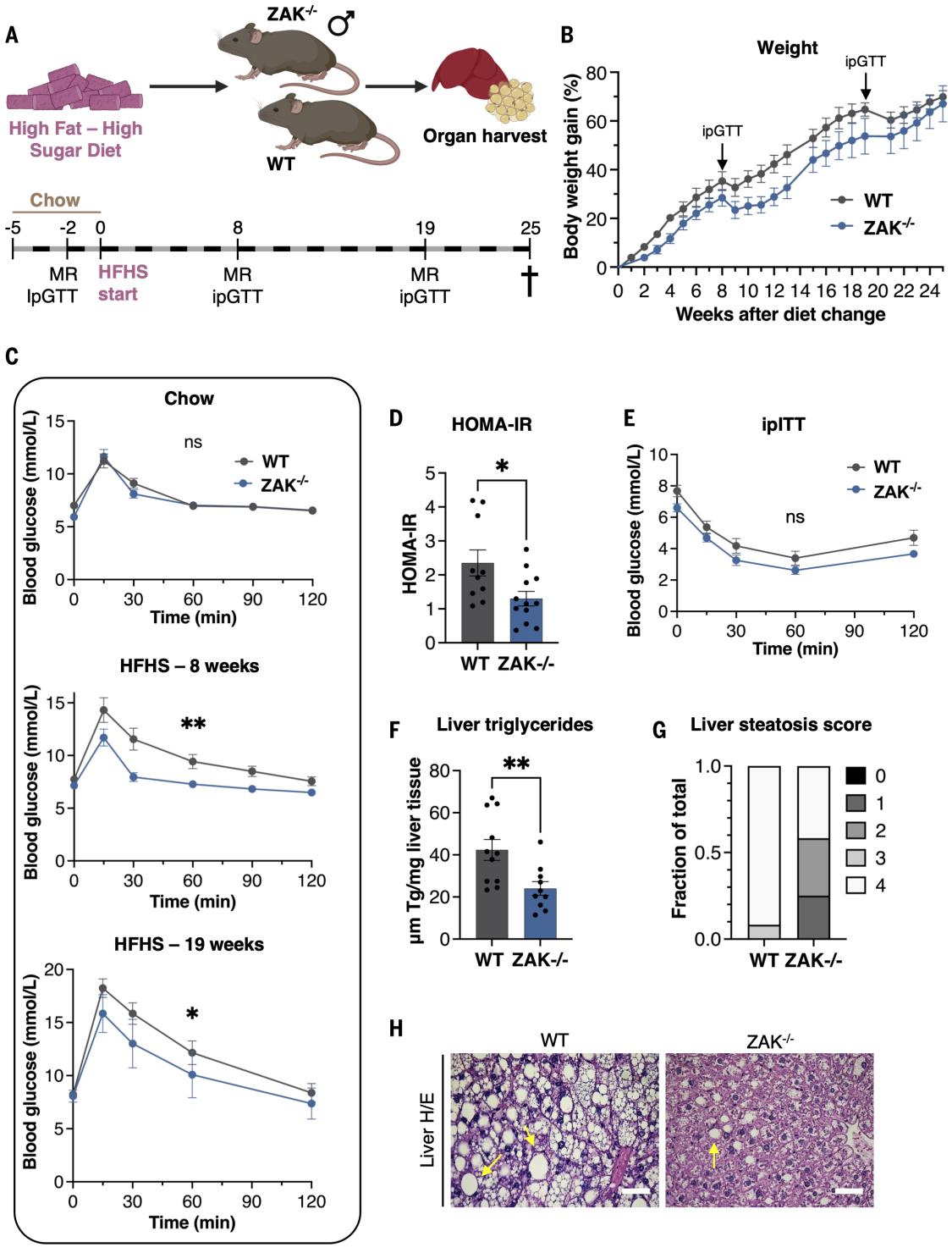

Fig. 4. ZAK$^{-/-}$ mice are protected against obesity-associated metabolic dysfunction. (**A**) Schematic of mouse feeding experiment. Ten- to 12-week-old male WT (n = 13) and ZAK$^{-/-}$ (n = 12) mice were maintained on chow and subjected to MR scanning and ipGTT 2 weeks before shifting to a HFHS diet. Mice were subjected to MR scanning and ipGTT after a further 8 and 19 weeks of HFHS feeding. Mice were euthanized and tissues were collected 25 weeks after the diet shift. (**B**) Percent body weight gain of mice from (A). Arrows mark the time of IpGTT assay and resulting transient weight loss. (**C**) Blood glucose concentrations of mice from (A) subjected to ipGTT assay. (**D**) HOMA-IR of mice from (A). (**E**) Blood glucose concentration of mice from fig. S4I subjected to the IpITT at the 8-week time point (WT, n = 12; ZAK$^{-/-}$, n = 7). (**F**) Liver triglyceride content of mice in (A). (**G**) Scoring of liver steatosis grade (scale, 0 to 4) of mice from (A). (**H**) Images of representative hematoxylin & eosin (H&E)–stained WT and ZAK$^{-/-}$ liver sections from mice in (A). Arrows indicate areas of steatosis. For (B) to (F), all data are plotted as mean and all error bars represent the SEM. For (C) and (E), statistical analysis is based on the area under the curve (AUC) for each experimental group. *$P \leq 0.05$; **$P \leq 0.01$ by Welch's t test in (D) and (F) and Mann-Whitney U test in (C) and (E). All scale bars, 50 µm.

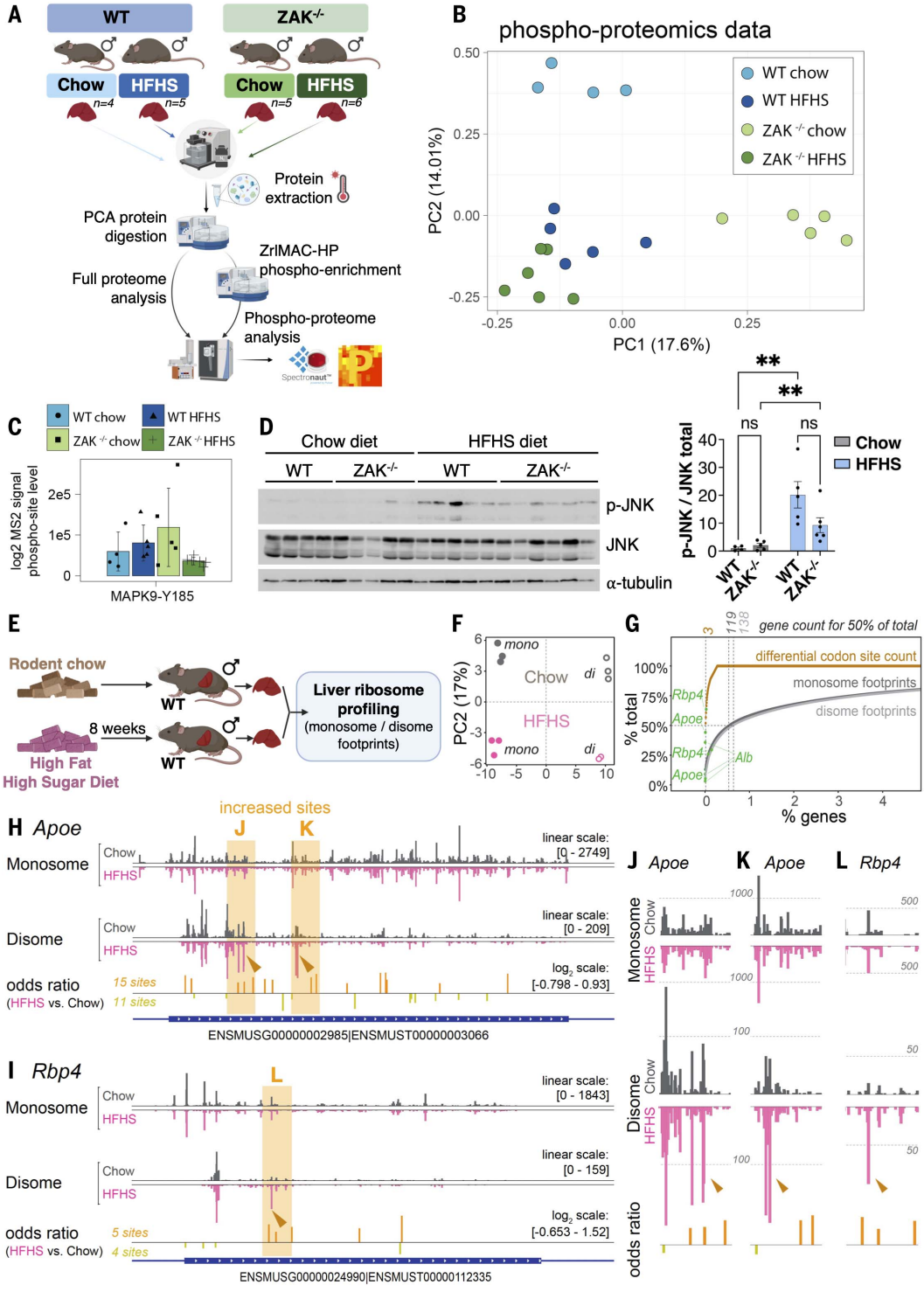

Fig. 5. Ribosome profiling of monosome and disome footprints reveals discreet changes to the translation landscape upon HFHS feeding. (**A**) Experimental design and workflow for proteomic and phosphoproteomic profiling of mouse livers. Ten- to 12-week-old mice of the indicated genotypes were fed chow or HFHS for 5 weeks (n = 4 to 6). (**B**) PCA of the phosphoproteomic profiles of mouse livers from (A). (**C**) Barplots of intensities derived from MS2 data for activation-associated phosphorylation sites on MAPK9 (JNK2). Height of the bars represents the average of the measurements and error bars the SE. Missing values in the MS data are plotted as zero values. (**D**) Lysates of livers from (A) were analyzed by immunoblotting with the indicated antibodies (left) and p-JNK divided by total JNK signals was quantified (right). Data are plotted as mean, and all error bars represent the SEM. *$P \leq 0.05$; **$P \leq 0.01$ by two-way ANOVA with Tukey's post hoc test. (**E**) Schematic of in vivo monosome and disome profiling experiment. Twelve-week-old male WT mice were fed normal chow or a HFHS diet for 8 weeks (n = 3). (**F**) PCA on monosome (closed circles) and disome (open circles) footprint data from individual mice, using the top 500 expressed genes. (**G**) Contribution of the most prominent genes to cumulative total signal for monosome footprints (dark gray), disome footprints (light gray), and differential codon sites from fig. S8C (orange). The locations of *Alb*, *Apoe*, and *Rbp4* in the cumulative datasets are highlighted. (**H**) Position-specific A-site signal for monosome and disome footprints across the *Apoe* mRNA for chow-fed (gray) and HFHS-fed (pink) conditions. Below monosome and disome tracks, positions of differential codon sites are depicted, with height corresponding to odds ratio values, and the same color coding is used as in fig. S8C. (**I**) As in (H) but for *Rbp4*. (**J**) Magnification of the left highlighted region of *Apoe* from (H) with high disome signal specifically in HFHS, and neighboring differential codon sites, consistent with increased collisions in this area. (**K**) As in (J) but for the right highlighted region. (**L**) As in (J) and (K) but for the high-disome site from the *Rbp4* transcript in (I).

signaling in WT mice likely occurs in steatotic hepatocytes, in which we managed to detect weak p-JNK positivity by immunohistochemistry (IHC) (fig. S7D). We also conducted a mouse experiment in which we fed WT and ZAK$^{-/-}$ mice either chow or HFHS for 16 weeks. These mice were starved overnight before euthanasia (*53*) and their livers analyzed for p-JNK by Western blotting (fig. S7E). This approach also failed to highlight deregulation of HFHS-associated JNK activity, which may be explained by our small sample size (fig. S7F).

Liver ribosome profiling reveals effects on global translation and distinct stalling and collision sites on highly expressed transcripts upon HFHS treatment

Using ribosome profiling (ribo-seq), we next investigated to what extent the HFHS diet–induced

phenotype was accompanied by translational alterations in liver (Fig. 5E). We prepared riboseq libraries from two footprint species: standard ~30 nt monosome-protected footprints and ~60 nt disome footprints, which are indicative of ribosomal stacking and collisions (*54*–*56*). Abundant disome footprints can be observed in mouse liver and at specific positions even under physiological conditions (*54*), likely diagnostic of sites of temporary translation slowdown that will not elicit a collision response such as the RSR. In our analyses, we aimed at identifying exacerbated disome coverage or new sites dependent on HFHS. First, PCA on footprint signal from the top 500 expressed genes indicated separation by library type (monosome or disome) followed by diet (chow or HFHS) (Fig. 5F). Monosome footprint analyses suggested that HFHS diet was not associated with strong systematic, transcriptome-wide effects on elongation kinetics, as indicated by footprint alignment to the 5′ and 3′ ends of coding sequences (fig. S8A) and an analysis of codon dwell times (*57*) (fig. S8B). Next, we extended our analyses to specific sites on the translatome. We calculated position-specific ribosome occupancies transcriptome-wide using a recently reported pause score metric (*58*, *59*), yielding 150 sites with increased and 160 sites with decreased relative ribosome occupancy in HFHS- versus chow-fed animals (fig. S8C, left panel). Many of these sites corresponded to positions on the translatome with high ribosomal occupancy (fig. S8C, right panel), so we explored the possibility that translational alterations affecting a relatively small number of sites on transcripts with very high translational volume could be associated with HFHS treatment. Thus, we quantified how individual high-expression genes contributed to overall translational activity in liver, which revealed a strong bias toward a few dominating transcripts, in particular mRNAs that encode bloodstream-secreted proteins such as albumin (*Alb*, 8.9% of all hepatic translation), apolipoprotein E (*Apoe*, 4.2%), and other mRNAs (Fig. 5G, dark gray curve; 119 genes make up 50% of all hepatic translation). A globally similar distribution was found for disome footprints (Fig. 5G, light gray curve). The group of differential codon sites showed an even stronger bias toward highly dominant transcripts, with three mRNAs, *Alb*, *Apoe*, and *Tfr*, accounting for half of the detected sites (Fig. 5G, orange curve, and table S3). To follow up on this observation, we inspected monosome and disome coverage and differential codon sites across the top-ranked transcripts. These analyses established that overall footprint distributions were highly similar and reproducible between HFHS- and chow-fed animals, as exemplified by the monosome and disome coverage patterns on *Alb* mRNA (fig. S8D). However, for some highly abundant mRNAs, such as *Apoe* (Fig. 5H) and retinol-binding protein 4 *(Rbp4*; Fig. 5I), we identified strongly enriched disome sites specifically in HFHS livers (Fig. 5, H and I, orange shading and arrows). Closer inspection of these transcript regions (Fig. 5, J to L) revealed that these disome positions were just upstream, in close proximity to increased differential sites from the monosome footprint odds ratio analysis, a constellation compatible with increased collisions at these sites.

ZAK$^{-/-}$ *mice are protected against metabolic decline in aging*

Male mice develop insulin resistance during aging (*60*), which at a very old age can be compensated for by pancreatic islet hypertrophy (*61*). Given the marked protection of ZAK$^{-/-}$ mice against metabolic dysfunction in obesity, we allowed chow-fed mice of both sexes to reach between 14 and 16 months of age before subjecting them to ipGTT (Fig. 6A). At this age, and similar to young mice, WT males were slightly heavier than their *Zak*-deleted counterparts (fig. S8E), whereas the weight of female mice was independent of genotype (fig. S8F). Aged male WT mice presented with a strongly impaired blood glucose control in ipGTT assay, as expected (Fig. 6B, top), whereas the performance of aged ZAK$^{-/-}$ male mice was undistinguishable from young male mice in this assay (Fig. 4C, top, and Fig. 6B, top). As previously reported (*60*), female mice did not present with pronounced aging-induced metabolic decline (Fig. 6B, bottom). The protection against aging-associated decline in glycemic control in ZAK$^{-/-}$ male mice was further underscored by reduced fasting blood glucose and insulin as well as lower HOMA-IR values (Fig. 6, C to E). Similar to early (8 weeks) HFHS-induced obesity (Fig. 4, C to E), these changes in males occurred in the absence of a measurable difference in whole-body insulin sensitivity assessed by an insulin tolerance test (fig. S8G). Inspection of the livers from these mice revealed different degrees of hepatic steatosis in three of seven WT mice, whereas only one of six ZAK$^{-/-}$ mice displayed the mildest degree of this hallmark of metabolic disease (Fig. 6, F and G), thus mirroring the genotype-specific characteristics of diet-induced obesity reported in Fig. 4.

These results suggest an overlap in the underlying metabolic stress signals in obesity and aging, albeit with a different magnitude and duration. To compare the extent of the oxidative burden of livers in the two conditions, we performed IHC to evaluate the content of 4-HNE in livers from young versus old and chow-fed versus HFHS-fed WT mice. 4-HNE is a commonly used marker of lipid peroxidation that has prognostic value in the diagnosis of NASH and other diseases associated with oxidative stress (*62*). Although IHC analysis of 4-HNE in young, chow-fed livers resulted only in homogeneous background staining (fig. S9A), the same analysis of HFHS-fed mice from Fig. 4A revealed a markedly increased overall staining, as well as the typical enrichment in steatotic areas around portal veins (*63*) (fig. S9B). These patterns were not observed in livers from aged mice (fig. S9C). This analysis indicates that oxidative stress load is increased in aged mouse livers but to a lesser extent than in HFHS-fed mice.

Deterioration of brown adipose tissue structure and function is attenuated in ZAK$^{-/-}$ *mice*

Adipose tissues undergo aging-induced deterioration in male mice as well as humans (*64*), including "whitening" of brown adipose tissue (BAT) (*65*). Compared with BAT sections from aged WT mice, the staining intensity of aged ZAK$^{-/-}$ mice more closely resembled that of BAT from young mice (fig. S10A, top and middle panels, and fig. S11A). These differences were also evident at the microscopic level, where the transition of multilocular BAT to a more unilocular WAT-like tissue was much more evident in old versus young WT samples compared with those from ZAK$^{-/-}$ mice (Fig. 6, H and I). Although the effects were in general smaller, we observed a similar protection against BAT whitening when reexamining our 25-week HFHS cohort (Fig. 4A; fig. S10, bottom panel; and fig. S11, A and B). These structural differences prompted us to evaluate functional BAT thermogenesis by infrared imaging of interscapular BAT on shaved mice. Although HFHS feeding was associated with the expected reduction of BAT temperature and thus thermogenesis in WT mice, ZAK$^{-/-}$ mice maintained a high temperature in this tissue (fig. S11, C and D).

Discussion

Here, we show that ROS potently interfere with ribosomal function in vitro, in human cell lines, and in mice. These aberrations activate the RSR pathway, culminating in oxidative stress-induced activation of the p38 and JNK kinases. This response has clear relevance for both pathological organismal responses to oxidative stress (zebrafish experiments) and physiological adaptations to increased ROS production. In mice, ROS-induced RSR signaling underlies at least some of the metabolic adaptations to high-fat diet–induced obesity and aging, such as the loss of glycemic control and development of hepatic steatosis. This is underscored by the protection of ZAK$^{-/-}$ mice against metabolic dysfunction when fed an HFHS diet, as well as the healthy metabolic aging observed in aged ZAK$^{-/-}$ male mice (Fig. 6J). The above insights highlight ribosomal impairment as an important metabolic stress signal used for the regulation of metabolism at an organismal level. Ribosomes are perfectly placed to perform the role of scaffolds

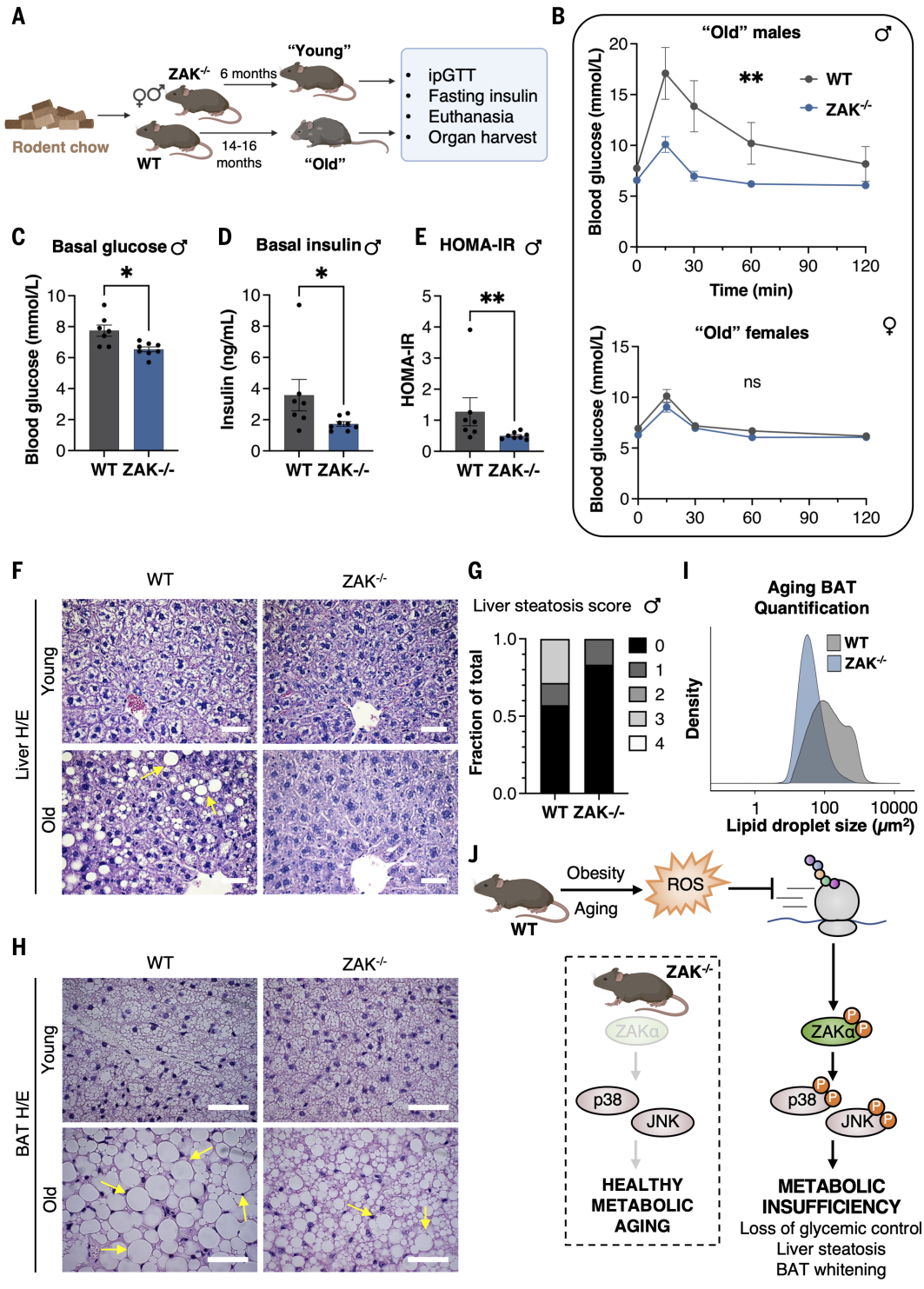

Fig. 6. Healthy metabolic aging in male ZAK$^{-/-}$ mice. (**A**) Schematic of mouse aging experiment. WT (male, n = 7; female, n = 16) and ZAK$^{-/-}$ (male, n = 7; female, n = 12) mice were maintained on a normal chow diet until 14 to 16 months of age ("old group"). Mice were subjected to ipGTT and euthanized 2 weeks later for collection of tissues. Tissues from 6-month-old WT and ZAK$^{-/-}$ male mice ("young group") were used for comparison. (**B**) Blood glucose concentrations of "old" male (top) and female (bottom) mice from (A) subjected to ipGTT assay. Statistical analysis is based on the AUC for each experimental group. (**C** to **E**) Basal glucose levels (C), basal insulin levels (D), and HOMA-IR (E) of fasted "old" male mice from (A). (**F**) Images of representative H&E-stained liver section from male mice in (A). Arrows indicate areas of steatosis. (**G**) Scoring of liver steatosis grade (scale, 0 to 4) of male mice from (A). (**H**) Images of representative H&E-stained sections of BAT from male mice in (A). Arrows indicate areas of notable lipid droplet condensation and BAT whitening. (**I**) Whole-mount BAT scans from (fig. S10A) were segmented according to lipid droplets. Individual droplet sizes for all aged WT and ZAK$^{-/-}$ samples were computed and represented in the form of histograms (n = 6). (**J**) Model of metabolic regulation by the RSR in obesity and aging in male mice. ROS produced as a result of HFHS feeding or during the course of aging impair ribosomal translation and activate the RSR sensor ZAKα. Downstream MAP kinase (p38 and JNK) signaling mediates features of metabolic decline such as glucose intolerance, liver steatosis, and BAT whitening. For (B) to (E), all data are plotted as mean and all error bars represent the SEM. *$P \leq 0.05$; **$P \leq 0.01$ by Welch's t test in (C) and by Mann-Whitney U test in (B), (D), and (E). All scale bars, 50 μm.

for mild stress signals in a broad context. Because they are present in high amounts in every cell and are constantly performing their function, compromised processivity of just a few ribosomes can provide for a highly sensitive and rapid readout of cellular perturbations (*39*). Previous work has highlighted oxidative damage to mRNA as a source of translational impairment (*39*), but our in vitro translation experiments highlight soluble cytoplasmic factors as the more sensitive components. These may include tRNAs and initiation and elongation factors. Although we did not obtain evidence of oxidative damage to the latter, we corroborated recently published evidence of ROS-induced tRNA cleavage and fragmentation (*43*). In addition to representing a depletion of key translation components, these fragments, likely generated by the RNase angiogenin, are generally considered to be inhibitory to ribosomal function (*41*, *42*).

JNK signaling promotes both insulin resistance and liver steatosis in obese mice (*14*). Specifically, mice conditionally deleted for JNK1 and JNK2 in the liver are protected against these outcomes when fed a high-fat diet (*19*). Among the relevant JNK targets is RXRα, the phosphorylation of which inhibits the PPARα complex and transcriptional activation of the *Fgf21* gene (*51*). FGF21 is a metabolic stress-induced hormone that has beneficial effects on both insulin sensitivity and liver adiposity (*66*), and these effects are exacerbated in *jnk*-deleted mice (*51*). Conversely, mice defective for p38 activation in the myeloid compartment are defective for hepatic FGF21 production and sensitized to metabolic dysfunction when fed a high-fat diet (*67*). A picture is emerging in which p38 and JNK signaling may compete for opposing outcomes depending on the tissue, cell type, and metabolic context. These intricacies likely allow for a fine-tuned mode of metabolic regulation that collectively manifests in an extremely well-buffered system. Unexpectedly, $ZAK^{-/-}$ mice, were protected against key aspects of metabolic dysfunction in the apparent absence of increased insulin sensitivity at intermediate time points (8 to 10 weeks). Alternative explanations may include stimulation of insulin-independent glucose uptake mechanisms and/or altered utilization of energy sources.

MAP3K ASK1 is a major ROS-induced activator of p38 and JNK in cell lines and mouse models (*44*) and has also been linked to metabolic regulation (*68*–*70*). Other ROS-activated MAP3Ks that have been implicated in metabolic control are MLK2/3 and MAP3K4 (*71*, *72*). In this work, we describe a clear protection of ZAK KO mice against HFHS-induced glucose intolerance and liver steatosis, and at least some of these phenotypes were related to ROS-mediated activation of ZAKα and the RSR. In one plausible model for the interplay of ZAKα and ASK1 in ROS-induced activation of p38 and JNK, ASK1 is the more relevant kinase upon sudden bursts of pathological levels of ROS, whereas ZAKα, through its ability to sense translational impairment, is more sensitive to the effects of slight elevations in intracellular ROS. Furthermore, the division of labor between these two kinases (as well as MLK2/3, MAP3K4, and potentially others) is likely tissue specific, because ZAKα levels in particular are highly variable among organs. It should be noted that the experimental systems used here differ widely in the source, duration, and magnitude of ROS exposure. In aggregate, we found that the role of ZAKα as the primary inducer of p38 and JNK activation and organismal protection was most evident in our experiments featuring excessive ROS levels in cell lines and zebrafish. In settings of prolonged exposure to lower levels of ROS (mouse obesity and aging), alternative mechanisms, as alluded to above, may play equally important roles. Additional work will be required to map the full inventory of ROS-activated MAP3 kinases and their relevance for ROS-driven physiological and pathological responses.

Next to glucose intolerance and stochastic liver steatosis, $ZAK^{-/-}$ male mice are also, at least partially, protected against BAT whitening and disruption of BAT integrity upon obesity and aging. These findings suggest that metabolic control exerted by the RSR pathway is not restricted to the liver, and that several tissues may contribute to the overall metabolic phenotypes of $ZAK^{-/-}$ mice. Indeed, a recent report described an independent role for the *Zak* gene in promoting stem cell plasticity in the small intestine of leucine-restricted mice (*73*). Further adding to the complexity of our current mouse model, the ZAKβ isoform is activated by volumetric cell compression and protects against muscle pathology in mice and humans (*49*, *74*), and this splice variant is also interrupted in the whole-body ZAK KO animals. For the present study, generation of mouse models for conditional KO of the *Zakα* isoform was not achieved. Future efforts in this direction will be crucial for uncovering the tissue-specific contributions of the RSR to the metabolic phenotypes that we describe. We also did not manage to detect *Zak*-dependent activation of p38 and JNK kinase isoforms in liver, adipose tissues, and other metabolically relevant organs. We suspect that the underlying technical explanation is a prolonged but weak overactivation of these stress kinases during HFHS feeding, which is difficult to detect with conventional methods because of high mouse-to-mouse variation. Although p38 and JNK are well-established effectors in the RSR, the lack of a direct signaling link from ZAKα to these kinases in vivo limits our conclusions regarding the mechanisms underlying metabolic protection of ZAK KO mice. Finally, we do not know to what extent our findings in mice can be extrapolated to humans. Patients with nonsense mutations in the common kinase domain of ZAKα and ZAKβ present with severe early-onset myopathy but with no reports of phenotypes of a metabolic nature (*74*). However, the feeding paradigm for mice used in this study is generally considered a good model of human obesity and associated metabolic complications. In humans, *Zakα* mRNA is robustly identified in all major metabolic tissues (see https://gtexportal.org/), so we consider it likely that the RSR also mediates metabolic adaptation in our own species.

In summary, our work uncovers a role of the ribosome as a signaling platform for metabolic regulation and highlights the RSR pathway as an important inducer of metabolic changes associated with obesity and aging. These findings may present opportunities for the development of therapeutic strategies to combat metabolic diseases.

Materials and methods summary

Polysome profiling

After cells were exposed to various treatments, cytosolic lysates were prepared using 20 mM HEPES, pH 7.5, 100 mM NaCl, 5 mM $MgCl_2$, 100 μg/ml digitonin, 100 μg/ml cycloheximide, 1× protease inhibitor cocktail (Sigma, catalog #P8340), and 200 U NxGen RNase inhibitor (Lucigen, catalog #30281). Extracts were incubated on ice for 5 min before centrifugation at 17,000*g* for 5 min at 4°C. After adding calcium chloride to a final concentration of 1 mM, lysates were optionally digested with 500 U MNase (New England Biolabs, catalog #M0247) for 30 min at 22°C. Digestion was terminated by adding 2 mM EGTA. Equivalent amounts of lysate (250 mg of undigested RNA or 350 to 400 mg of MNase-digested RNA) were resolved on 15 to 50% sucrose gradients. Gradients were centrifuged at 38,000 rpm in a Sorvall TH64.1 rotor for 2 hours at 4°C. The gradients were passed through an ISCO density gradient fractionation system with continuous monitoring of the absorbance at 254 nm.

Reconstituted in vitro translation

Translation reactions were reconstituted by mixing one part isolated ribosomes, five parts cytoplasmic lysates, one part in vitro transcribed luciferase mRNA (final concentration 1 to 10 ng/μl), and three parts translation buffer [final concentrations of 1.6 mM HEPES, 10 mM creatine phosphate (Sigma Aldrich, catalog #27920), 50 ng/μl creatine kinase (Sigma Aldrich, catalog #10127566001), 10 μM spermidine (Sigma Aldrich, catalog # S0266), 10 μM amino acids (Promega, catalog # L4461), 65 mM KAc, 0.75 mM $MgAc_2$, and murine RNase inhibitor]. Luciferase mRNA with an EMCV IRES was transcribed from a plasmid using HiScribe T7 ARCA mRNA Kit with tailing (New England Biolabs, catalog #E2060) according to manufacturer's specifications. Translation reactions were incubated at 37°C for 30 min, and translational output was measured as luciferase activity detected with Dual-Glo Luciferase Assay System (Promega, catalog #E2940) according to the manufacturer's specifications. For H_2O_2 treatment, fractions were treated with 5 mM H_2O_2 (Sigma-Aldrich, catalog #H1009) for 10 min at 25°C, followed by treatment with either 1 μg/μl catalase (Sigma-Aldrich, C1345-1G) or vehicle (1 mM potassium phosphate). For UV irradiation, fractions were irradiated with 500 J/m^2 UVB and immediately added to the in vitro translation reaction.

Menadione treatment of zebrafish larvae

Freshly collected zebrafish eggs were incubated in E3 medium (5 mM NaCl, 0.17 mM KCl, 0.33 mM $CaCl_2$, 0.33 mM $MgSO_4$, and 0.00001%

methylene blue). Unfertilized and dead eggs were removed, and embryos around the early gastrula stage, ~6 hours postfertilization, were randomly distributed into 12-well plates with 10 embryos per well. Menadione powder was dissolved as a 25 mM stock solution in E3 medium and diluted to a working concentration of 9 μM in E3 with or without 60 μM NAC. This medium was refreshed daily, and dead eggs were removed. To enforce full hatching of all genotypes, 1 day postfertilization (dpf) eggs were incubated overnight with 6 μg/ml Pronase (Sigma-Aldrich, catalog #10165921001). Embryos were scored as dead in the absence of a beating heart. Darkened yolk, cardiac edema, or shortened tails were scored as teratogenic (developmental) effects. All larvae were euthanized at maximally 5 dpf.

Mouse experiments

ZAK KO mice were on a mixed C57BL/6NJ background. Experimental cohorts of WT and ZAK KO mice were obtained by in-house breeding of heterozygotes. For feeding experiments, young male littermate mice with an age span of 10 to 15 weeks of age were used. Body weight and food intake were measured weekly. Fresh HFHS food pellets were provided to the mice once per week. For NAC supplementation, the compound was added directly to the drinking water at 10 g per liter, and the solution was refreshed three times per week. Body composition was determined by quantitative MR using the 4in1 Body Composition Analyzer (EchoMRI). In the aging cohort, male and female mice were group caged according to their sex with ad libitum access to chow diet and water, subjected to ipGTT analysis at 13 to 15 months of age, and euthanized and dissected 1 month later.

Ribosome profiling (monosome and disome) of mouse livers

Livers were harvested and flash-frozen in liquid nitrogen. Starting with 200-mg liver pieces from individual animals, lysates and ribosome footprints were generated by RNase I digestion and purified. Briefly, 5 μg of RNase I-digested RNA was separated on 15% urea-polyacrylamide gels to excise monosome (~30 nt) and disome (~60 nt) footprints. From the gel slices, RNA was extracted overnight at 4°C on a rotating wheel before precipitation in isopropanol for 3 hours at −20°C. RNA 3′-end repair was performed with 2 U/μl of T4 PNK (Lucigen) before a 2 hours of adapter ligation at 25°C using T4 RNA Ligase 1 (NEB) and T4 RNA Ligase 2 Deletion Mutant (Lucigen) and 1 μl of a 20 μM 5′-adenylated DNA adapter. Adapter removal was performed by treating individual libraries with 5′deadenylase (NEB) and RecJf exonuclease (NEB) for 1 hour at 30°C and 1 hour at 37°C. Using Zymo Clean & Concentrator columns, samples were purified and pooled. Ribosomal RNA was depleted according to siTools Biotech rRNA depletion kit specifications with a custom-made riboPOOL. The clean-up step was performed using Zymo Clean & Concentrator columns. Further library preparation steps were performed as described. The amplification of libraries was performed using i5 and i7 [NexteraD502 or NexteraD503 (monosomes) and NexteraD504 or NexteraD505 (disomes)] primers. Libraries were sequenced on a NovaSeq6000 (Illumina).

REFERENCES AND NOTES

1. B. H. Goodpaster, L. M. Sparks, Metabolic flexibility in health and disease. *Cell Metab.* **25**, 1027–1036 (2017). doi: 10.1016/j.cmet.2017.04.015; pmid: 28467922
2. R. L. Smith, M. R. Soeters, R. C. I. Wüst, R. H. Houtkooper, Metabolic flexibility as an adaptation to energy resources and requirements in health and disease. *Endocr. Rev.* **39**, 489–517 (2018). doi: 10.1210/er.2017-00211; pmid: 29697773
3. B. A. Swinburn *et al.*, The global obesity pandemic: Shaped by global drivers and local environments. *Lancet* **378**, 804–814 (2011). doi: 10.1016/S0140-6736(11)60813-1; pmid: 21872749
4. T. D. Müller, M. Blüher, M. H. Tschöp, R. D. DiMarchi, Anti-obesity drug discovery: Advances and challenges. *Nat. Rev. Drug Discov.* **21**, 201–223 (2022). doi: 10.1038/s41573-021-00337-8; pmid: 34815532
5. M. Blüher, Obesity: Global epidemiology and pathogenesis. *Nat. Rev. Endocrinol.* **15**, 288–298 (2019). doi: 10.1038/s41574-019-0176-8; pmid: 30814686
6. M. W. Schwartz *et al.*, Obesity pathogenesis: An Endocrine Society scientific statement. *Endocr. Rev.* **38**, 267–296 (2017). doi: 10.1210/er.2017-00111; pmid: 28898979
7. A. K. Palmer, M. D. Jensen, Metabolic changes in aging humans: Current evidence and therapeutic strategies. *J. Clin. Invest.* **132**, e158451 (2022). doi: 10.1172/JCI158451; pmid: 35968789
8. T. Finkel, The metabolic regulation of aging. *Nat. Med.* **21**, 1416–1423 (2015). doi: 10.1038/nm.3998; pmid: 26646498
9. S. Furukawa *et al.*, Increased oxidative stress in obesity and its impact on metabolic syndrome. *J. Clin. Invest.* **114**, 1752–1761 (2004). doi: 10.1172/JCI21625; pmid: 15599400
10. H. J. Shields, A. Traa, J. M. Van Raamsdonk, Beneficial and detrimental effects of reactive oxygen species on lifespan: A comprehensive review of comparative and experimental studies. *Front. Cell Dev. Biol.* **9**, 628157 (2021). doi: 10.3389/fcell.2021.628157; pmid: 33644065
11. M. Schieber, N. S. Chandel, ROS function in redox signaling and oxidative stress. *Curr. Biol.* **24**, R453–R462 (2014). doi: 10.1016/j.cub.2014.03.034; pmid: 24845678
12. E. F. Wagner, A. R. Nebreda, Signal integration by JNK and p38 MAPK pathways in cancer development. *Nat. Rev. Cancer* **9**, 537–549 (2009). doi: 10.1038/nrc2694; pmid: 19629069
13. B. Canovas, A. R. Nebreda, Diversity and versatility of p38 kinase signalling in health and disease. *Nat. Rev. Mol. Cell Biol.* **22**, 346–366 (2021). doi: 10.1038/s41580-020-00322-w; pmid: 33504982
14. I. Nikolic, M. Leiva, G. Sabio, The role of stress kinases in metabolic disease. *Nat. Rev. Endocrinol.* **16**, 697–716 (2020). doi: 10.1038/s41574-020-00418-5; pmid: 33067545
15. G. Sumara *et al.*, Regulation of PKD by the MAPK p38delta in insulin secretion and glucose homeostasis. *Cell* **136**, 235–248 (2009). doi: 10.1016/j.cell.2008.11.018; pmid: 19135240
16. M. Leiva, N. Matesanz, M. Pulgarín-Alfaro, I. Nikolic, G. Sabio, Uncovering the Role of p38 Family Members in Adipose Tissue Physiology. *Front. Endocrinol. (Lausanne)* **11**, 572089 (2020). doi: 10.3389/fendo.2020.572089; pmid: 33424765
17. B. Cicuéndez, I. Ruiz-Garrido, A. Mora, G. Sabio, Stress kinases in the development of liver steatosis and hepatocellular carcinoma. *Mol. Metab.* **50**, 101190 (2021). doi: 10.1016/j.molmet.2021.101190; pmid: 33588102
18. G. Sabio *et al.*, A stress signaling pathway in adipose tissue regulates hepatic insulin resistance. *Science* **322**, 1539–1543 (2008). doi: 10.1126/science.1160794; pmid: 19056984
19. G. Tuncman *et al.*, Functional in vivo interactions between JNK1 and JNK2 isoforms in obesity and insulin resistance. *Proc. Natl. Acad. Sci. U.S.A.* **103**, 10741–10746 (2006). doi: 10.1073/pnas.0603509103; pmid: 16818881
20. A. C. Vind, A. V. Genzor, S. Bekker-Jensen, Ribosomal stress-surveillance: Three pathways is a magic number. *Nucleic Acids Res.* **48**, 10648–10661 (2020). doi: 10.1093/nar/gkaa757; pmid: 32941609
21. A. C. Vind *et al.*, ZAKα Recognizes Stalled Ribosomes through Partially Redundant Sensor Domains. *Mol. Cell* **78**, 700–713.e7 (2020). doi: 10.1016/j.molcel.2020.03.021; pmid: 32289254
22. C. C. Wu, A. Peterson, B. Zinshteyn, S. Regot, R. Green, Ribosome Collisions Trigger General Stress Responses to Regulate Cell Fate. *Cell* **182**, 404–416.e14 (2020). doi: 10.1016/j.cell.2020.06.006; pmid: 32610081
23. G. Snieckute *et al.*, Ribosome stalling is a signal for metabolic regulation by the ribotoxic stress response. *Cell Metab.* **34**, 2036–2046.e8 (2022). doi: 10.1016/j.cmet.2022.10.011; pmid: 36384144
24. M. S. Iordanov *et al.*, Ribotoxic stress response: Activation of the stress-activated protein kinase JNK1 by inhibitors of the peptidyl transferase reaction and by sequence-specific RNA damage to the alpha-sarcin/ricin loop in the 28S rRNA. *Mol. Cell. Biol.* **17**, 3373–3381 (1997). doi: 10.1128/MCB.17.6.3373; pmid: 9154836
25. D. Y. Ouyang, Y. Y. Wang, Y. T. Zheng, Activation of c-Jun N-terminal kinases by ribotoxic stresses. *Cell. Mol. Immunol.* **2**, 419–425 (2005). pmid: 16426491
26. X. Wang *et al.*, Complete inhibition of anisomycin and UV radiation but not cytokine induced JNK and p38 activation by an aryl-substituted dihydropyrrolopyrazole quinoline and mixed lineage kinase 7 small interfering RNA. *J. Biol. Chem.* **280**, 19298–19305 (2005). doi: 10.1074/jbc.M413059200; pmid: 15737997
27. K. S. Robinson *et al.*, ZAKα-driven ribotoxic stress response activates the human NLRP1 inflammasome. *Science* **377**, 328–335 (2022). doi: 10.1126/science.abl6324; pmid: 35857590
28. D. Shenton *et al.*, Global translational responses to oxidative stress impact upon multiple levels of protein synthesis. *J. Biol. Chem.* **281**, 29011–29021 (2006). doi: 10.1074/jbc.M601545200; pmid: 16849329
29. J. A. McCubrey, M. M. Lahair, R. A. Franklin, Reactive oxygen species-induced activation of the MAP kinase signaling pathways. *Antioxid. Redox Signal.* **8**, 1775–1789 (2006). doi: 10.1089/ars.2006.8.1775; pmid: 16987031
30. M. Stoneley *et al.*, Unresolved stalled ribosome complexes restrict cell-cycle progression after genotoxic stress. *Mol. Cell* **82**, 1557–1572.e7 (2022). doi: 10.1016/j.molcel.2022.01.019; pmid: 35180429
31. A. M. Darnell, A. R. Subramaniam, E. K. O'Shea, Translational control through differential ribosome pausing during amino acid limitation in mammalian cells. *Mol. Cell* **71**, 229–243.e11 (2018). doi: 10.1016/j.molcel.2018.06.041; pmid: 30029003
32. N. T. Ingolia, L. F. Lareau, J. S. Weissman, Ribosome profiling of mouse embryonic stem cells reveals the complexity and dynamics of mammalian proteomes. *Cell* **147**, 789–802 (2011). doi: 10.1016/j.cell.2011.10.002; pmid: 22056041
33. S. Juszkiewicz *et al.*, Ribosome collisions trigger cis-acting feedback inhibition of translation initiation. *eLife* **9**, e60038 (2020). doi: 10.7554/eLife.60038; pmid: 32657267
34. N. K. Sinha *et al.*, EDF1 coordinates cellular responses to ribosome collisions. *eLife* **9**, e58828 (2020). doi: 10.7554/eLife.58828; pmid: 32744497
35. S. Juszkiewicz, R. S. Hegde, Initiation of quality control during poly(A) translation requires site-specific ribosome ubiquitination. *Mol. Cell* **65**, 743–750.e4 (2017). doi: 10.1016/j.molcel.2016.11.039; pmid: 28065601
36. E. Sundaramoorthy *et al.*, ZNF598 and RACK1 regulate mammalian ribosome-associated quality control function by mediating regulatory 40S ribosomal ubiquitylation. *Mol. Cell* **65**, 751–760.e4 (2017). doi: 10.1016/j.molcel.2016.12.026; pmid: 28132843
37. A. Garzia, C. Meyer, T. Tuschl, The E3 ubiquitin ligase RNF10 modifies 40S ribosomal subunits of ribosomes compromised in translation. *Cell Rep.* **36**, 109468 (2021). doi: 10.1016/j.celrep.2021.109468; pmid: 34348161
38. D. M. Garshott *et al.*, iRQC, a surveillance pathway for 40S ribosomal quality control during mRNA translation initiation. *Cell Rep.* **36**, 109642 (2021). doi: 10.1016/j.celrep.2021.109642; pmid: 34469731
39. K. Q. Kim, H. S. Zaher, Canary in a coal mine: Collided ribosomes as sensors of cellular conditions. *Trends Biochem. Sci.* **47**, 82–97 (2022). doi: 10.1016/j.tibs.2021.09.001; pmid: 34607755
40. J. R. Burgoyne, P. Eaton, Contemporary techniques for detecting and identifying proteins susceptible to reversible thiol oxidation. *Biochem. Soc. Trans.* **39**, 1260–1267 (2011). doi: 10.1042/BST0391260; pmid: 21936799
41. S. Yamasaki, P. Ivanov, G. F. Hu, P. Anderson, Angiogenin cleaves tRNA and promotes stress-induced translational repression. *J. Cell Biol.* **185**, 35–42 (2009). doi: 10.1083/jcb.200811106; pmid: 19332886

42. H. Fu *et al*., Stress induces tRNA cleavage by angiogenin in mammalian cells. *FEBS Lett.* **583**, 437–442 (2009). doi: 10.1016/j.febslet.2008.12.043; pmid: 19114040
43. Y. Akiyama *et al*., RTCB complex regulates stress-induced tRNA cleavage. *Int. J. Mol. Sci.* **23**, 13100 (2022). doi: 10.3390/ijms232113100; pmid: 36361884
44. S. Shiizaki, I. Naguro, H. Ichijo, Activation mechanisms of ASK1 in response to various stresses and its significance in intracellular signaling. *Adv. Biol. Regul.* **53**, 135–144 (2013). doi: 10.1016/j.jbior.2012.09.006; pmid: 23031789
45. E. E. Patton, L. I. Zon, D. M. Langenau, Zebrafish disease models in drug discovery: From preclinical modelling to clinical trials. *Nat. Rev. Drug Discov.* **20**, 611–628 (2021). doi: 10.1038/s41573-021-00210-8; pmid: 34117457
46. P. Giansanti *et al*., Mass spectrometry-based draft of the mouse proteome. *Nat. Methods* **19**, 803–811 (2022). doi: 10.1038/s41592-022-01526-y; pmid: 35710609
47. P. Ranea-Robles, J. Lund, C. Clemmensen, The physiology of experimental overfeeding in animals. *Mol. Metab.* **64**, 101573 (2022). doi: 10.1016/j.molmet.2022.101573; pmid: 35970448
48. N. Matsuzawa-Nagata *et al*., Increased oxidative stress precedes the onset of high-fat diet-induced insulin resistance and obesity. *Metabolism* **57**, 1071–1077 (2008). doi: 10.1016/j.metabol.2008.03.010; pmid: 18640384
49. C. Nordgaard *et al*., ZAKβ is activated by cellular compression and mediates contraction-induced MAP kinase signaling in skeletal muscle. *EMBO J.* **41**, e111650 (2022). doi: 10.15252/embj.2022111650; pmid: 35899396
50. M. T. F. Damgaard *et al*., Age-dependent alterations of glucose clearance and homeostasis are temporally separated and modulated by dietary fat. *J. Nutr. Biochem.* **54**, 66–76 (2018). doi: 10.1016/j.jnutbio.2017.09.026; pmid: 29268121
51. S. Vernia *et al*., Phosphorylation of RXRα mediates the effect of JNK to suppress hepatic FGF21 expression and promote metabolic syndrome. *Proc. Natl. Acad. Sci. U.S.A.* **119**, e2210434119 (2022). doi: 10.1073/pnas.2210434119; pmid: 36282921
52. J. F. Pei *et al*., Diurnal oscillations of endogenous H_2O_2 sustained by $p66^{Shc}$ regulate circadian clocks. *Nat. Cell Biol.* **21**, 1553–1564 (2019). doi: 10.1038/s41556-019-0420-4; pmid: 31768048
53. S. Vernia *et al*., The PPARα-FGF21 hormone axis contributes to metabolic regulation by the hepatic JNK signaling pathway. *Cell Metab.* **20**, 512–525 (2014). doi: 10.1016/j.cmet.2014.06.010; pmid: 25043817
54. A. B. Arpat *et al*., Transcriptome-wide sites of collided ribosomes reveal principles of translational pausing. *Genome Res.* **30**, 985–999 (2020). doi: 10.1101/gr.257741.119; pmid: 32703885
55. S. Meydan, N. R. Guydosh, Disome and Trisome Profiling Reveal Genome-wide Targets of Ribosome Quality Control. *Mol. Cell* **79**, 588–602.e6 (2020). doi: 10.1016/j.molcel.2020.06.010; pmid: 32615089
56. T. Zhao *et al*., Disome-seq reveals widespread ribosome collisions that promote cotranslational protein folding. *Genome Biol.* **22**, 16 (2021). doi: 10.1186/s13059-020-02256-0; pmid: 33402206
57. C. Gobet, F. Naef, Ribo-DT: An automated pipeline for inferring codon dwell times from ribosome profiling data. *Methods* **203**, 10–16 (2022). doi: 10.1016/j.ymeth.2021.10.004; pmid: 34673173
58. K. C. Stein, A. Kriel, J. Frydman, Nascent polypeptide domain topology and elongation rate direct the cotranslational hierarchy of Hsp70 and TRiC/CCT. *Mol. Cell* **75**, 1117–1130.e5 (2019). doi: 10.1016/j.molcel.2019.06.036; pmid: 31400849
59. K. C. Stein, F. Morales-Polanco, J. van der Lienden, T. K. Rainbolt, J. Frydman, Ageing exacerbates ribosome pausing to disrupt cotranslational proteostasis. *Nature* **601**, 637–642 (2022). doi: 10.1038/s41586-021-04295-4; pmid: 35046576
60. T. H. Reynolds *et al*., The impact of age and sex on body composition and glucose sensitivity in C57BL/6J mice. *Physiol. Rep.* **7**, e13995 (2019). doi: 10.14814/phy2.13995; pmid: 30706674
61. E. Tudurí *et al*., The effects of aging on male mouse pancreatic beta-cell function involve multiple events in the regulation of secretion: Influence of insulin sensitivity. *J. Gerontol. A Biol. Sci. Med. Sci.* **77**, 405–415 (2022). doi: 10.1093/gerona/glab276; pmid: 34562079
62. S. Dalleau, M. Baradat, F. Guéraud, L. Huc, Cell death and diseases related to oxidative stress: 4-hydroxynonenal (HNE) in the balance. *Cell Death Differ.* **20**, 1615–1630 (2013). doi: 10.1038/cdd.2013.138; pmid: 24096871
63. M. J. Ronis *et al*., Increased 4-hydroxynonenal protein adducts in male GSTA4-4/PPAR-α double knockout mice enhance injury during early stages of alcoholic liver disease. *Am. J. Physiol. Gastrointest. Liver Physiol.* **308**, G403–G415 (2015). doi: 10.1152/ajpgi.00154.2014; pmid: 25501545
64. M. Schosserer, J. Grillari, C. Wolfrum, M. Scheideler, Age-induced changes in white, brite, and brown adipose depots: A mini-review. *Gerontology* **64**, 229–236 (2018). doi: 10.1159/000485183; pmid: 29212073
65. L. F. Gonçalves *et al*., Ageing is associated with brown adipose tissue remodelling and loss of white fat browning in female C57BL/6 mice. *Int. J. Exp. Pathol.* **98**, 100–108 (2017). doi: 10.1111/iep.12228; pmid: 28543963
66. J. Silva *et al*., Ribosome impairment regulates intestinal stem cell identity via ZAKa activation. *Nat. Commun.* **13**, 4492 (2022). doi: 10.1038/s41467-022-32220-4; pmid: 35918345
67. N. Vasli *et al*., Recessive mutations in the kinase ZAK cause a congenital myopathy with fibre type disproportion. *Brain* **140**, 37–48 (2017). doi: 10.1093/brain/aww257; pmid: 27816943
68. S. Keipert, M. Ost, Stress-induced FGF21 and GDF15 in obesity and obesity resistance. *Trends Endocrinol. Metab.* **32**, 904–915 (2021). doi: 10.1016/j.tem.2021.08.008; pmid: 34526227
69. M. Crespo *et al*., Myeloid p38 activation maintains macrophage-liver crosstalk and BAT thermogenesis through IL-12-FGF21 axis. *Hepatology* **77**, 874–887 (2023). doi: 10.1002/hep.32581; pmid: 35592906
70. T. D. Challa *et al*., Liver ASK1 protects from non-alcoholic fatty liver disease and fibrosis. *EMBO Mol. Med.* **11**, e10124 (2019). doi: 10.15252/emmm.201810124; pmid: 31595673
71. F. C. Lucchini *et al*., ASK1 inhibits browning of white adipose tissue in obesity. *Nat. Commun.* **11**, 1642 (2020). doi: 10.1038/s41467-020-15483-7; pmid: 32242025
72. E. Yamamoto *et al*., Olmesartan prevents cardiovascular injury and hepatic steatosis in obesity and diabetes, accompanied by apoptosis signal regulating kinase-1 inhibition. *Hypertension* **52**, 573–580 (2008). doi: 10.1161/HYPERTENSIONAHA.108.112292; pmid: 18678790
73. S. M. Craige, M. M. Reif, S. Kant, Mixed - Lineage Protein kinases (MLKs) in inflammation, metabolism, and other disease states. *Biochim. Biophys. Acta* **1862**, 1581–1586 (2016). doi: 10.1016/j.bbadis.2016.05.022; pmid: 27259981
74. Z. He *et al*., Identification of MAP3K4 as a novel regulation factor of hepatic lipid metabolism in non-alcoholic fatty liver disease. *J. Transl. Med.* **20**, 529 (2022). doi: 10.1186/s12967-022-03734-8; pmid: 36376950
75. Y. Perez-Riverol *et al*., The PRIDE database resources in 2022: A hub for mass spectrometry-based proteomics evidences. *Nucleic Acids Res.* **50** (D1), D543–D552 (2022). doi: 10.1093/nar/gkab1038; pmid: 34723319
76. M. Leleu, R. Dreos, Monosome and disome profiling of livers from HFHS-fed mice, Zenodo (2023); https://doi.org/10.5281/zenodo.8309532.

ACKNOWLEDGMENTS

We thank P. Rengtved Lundegaard (University of Copenhagen, Denmark) for help with zebrafish work, X. Lu (Jinan University, China) for the kind gift of ZAK inhibitors, V. Li (Crick Institute, United Kingdom) for providing access to the ZAK KO mouse strain, and the Department of Experimental Medicine (University of Copenhagen, Denmark) for help with housing of mice and zebrafish. **Funding:** Work in S.B.-J.'s laboratory was supported by grants from the Novo Nordisk Foundation (grant NNF21OC0071475), the Nordea Foundation, and the European Research Council (ERC) under the European Union's Horizon 2020 research and innovation program (grant 863911, PHYRIST). Center for Gene Expression (CGEN) is a Center of Excellence funded by The National Danish Research Foundation (grant DNRF166). A.C.V. is supported by the BRIDGE – Translational Excellence Program funded by the Novo Nordisk Foundation (grant NNF20SA0064340). The Novo Nordisk Foundation Center for Basic Metabolic Research is an independent Research Center based at the University of Copenhagen, Denmark, and is partially funded by an unconditional donation from the Novo Nordisk Foundation (www.cbmr.ku.dk) (grant NNF18CC0034900). D.M.S. is supported by the Swiss National Science Foundation through the National Center of Competence in Research RNA & Disease (grant 141735 and individual grant 179190). A.E.W. and M.S. are supported by the Medical Research Council, UK through MRC program core funding (grant 5TR00). Work in B.A.H.J.'s laboratory was funded by the Novo Nordisk Foundation (grant NNF21OC0066931). Work in J.V.O.'s laboratory at The Novo Nordisk Foundation Center for Protein Research (CPR) is funded in part by a generous donation from the Novo Nordisk Foundation (grant NNF14CC0001). **Author contributions:** S.B.-J., G.S., L.R., and A.C.V. conceived the study. G.S., L.R., A.C.V., Z.W., F.S.A., M.S., S.C., A.M.V., M.L., R.D., A.R., D.M.G., A.V.G., B.S.-Y.C., A.L.B., F.S., M.D., L.C.M.D., M.B., and S.S.P. performed experiments and analyzed data. A.E.W., A.H.L., J.T.T., J.V.O., M.E.P., B.A.H.J., C.C., Z.G.-H., D.G., and S.B.-J. supervised experiments and provided data interpretation. S.B.-J. wrote the manuscript with input from D.G. **Competing interests:** The authors declare no competing interests. **Data and materials availability:** The mass spectrometry proteomics data have been deposited to the ProteomeXchange Consortium through the PRIDE (75) partner repository with the dataset identifier PXD043071. Sequencing data files have been deposited in NCBI Gene Expression Omnibus (GEO) with the accession code GSE235700. The scripts for data analysis have been deposited on Zenodo (76). All other data are available in the main text or the supplementary materials. Plasmids and cell lines generated in this study are available upon request and without the need for a material transfer agreement.

SUPPLEMENTARY MATERIALS

science.org/doi/10.1126/science.adf3208
Materials and Methods
Figs. S1 to S11
References (*77*–*89*)
MDAR Reproducibility Checklist
Tables S1 to S3

Submitted 13 October 2022; resubmitted 4 July 2023
Accepted 3 November 2023
10.1126/science.adf3208

ROS-induced ribosome impairment underlies ZAK#-mediated metabolic decline in obesity and aging

Goda Snieckute, Laura Ryder, Anna Constance Vind, Zhenzhen Wu, Frederic Schrøder Arendrup, Mark Stoneley, Sébastien Chamois, Ana Martinez-Val, Marion Leleu, René Dreos, Alexander Russell, David Michael Gay, Aitana Victoria Genzor, Beatrice So-Yun Choi, Astrid Linde Basse, Frederike Sass, Morten Dall, Lucile Chantal Marie Dollet, Melanie Blasius, Anne E. Willis, Anders H. Lund, Jonas T. Treebak, Jesper Velgaard Olsen, Steen Seier Poulsen, Mary Elizabeth Pownall, Benjamin Anderschou Holbech Jensen, Christoffer Clemmensen, Zach Gerhart-Hines, David Gatfield, and Simon Bekker-Jensen

Science **382** (6675), eadf3208. DOI: 10.1126/science.adf3208

Editor's summary

Under conditions of food scarcity, metabolic flexibility was historically important for humans to optimize storage and access to energy when food was not readily available. By contrast, the constant access to high-calorie foods in modern societies has become a liability, contributing to the rise in obesity and metabolic diseases. Reactive oxygen species are thought to contribute to the metabolic dysregulation associated with obesity and aging, but the underlying process was not well understood. Snieckute *et al*. have now identified a mechanism linking reactive oxygen species, a protein called ZAK#, and resulting changes in ribosome function, which then contribute to the observed metabolic changes across multiple model animal species. —Yevgeniya Nusinovich